Electronic Supplementary Material (ESI) for Journal of Materials Chemistry A.

Supporting information

Green biopolymer-CNT films exhibit high thermoelectric power factor and electrical conductivity for low temperature heat energy harvesting

Yizhuo Wang[1], Kuncai Li[1], Jing Wang[1], Xu Dai[1], Xu Sun[1], Daotong Chong[1,2], Junjie Yan[1,2], Liuyang Zhang[3], Hong Wang[1,2]*

[1] State Key Laboratory of Multiphase Flow in Power Engineering & Frontier Institute of Science and Technology, Xi'an Jiaotong University, Xi'an, 710054, China

[2]School of Energy and Power Engineering, Xi'an Jiaotong University, Xi'an, 710054, China

[3]School of Mechanical Engineering, Xi'an Jiaotong University, Xi'an, 710054, China

E-mail: hong.wang@xjtu.edu.cn

EXPERIMENTAL SECTION

Materials

SWCNT-XFS16 and SWCNT-XFS22 were purchased from Nanjing XFNANO Materials Tech. Co. Ltd, China. Polyethyleneimine (PEI) (99%) was purchased from MACKLIN Co., Ltd, China. Diethylenetriamine (DETA) (99%) was purchased from ENERGY CHEMICAL Co., Ltd., China. 1,3-Dimethyl-2-phenyl-2,3-dihydro-1H-benzoimidazole (N-DMBI) (98%) was purchased from Sigma-Aldrich Co., Ltd., U.S.A. Dimethyl sulfoxide was purchased from MACKLIN Co., Ltd, China. Methylene chloride was purchased from sinopharm Chemical Reagent Co., Ltd.

Preparation of CNT/ willow catkin composites films：

The preparation process was shown in Figure 1a. Willow catkins were pretreated according to previously reported literature.[1] 5 mg carbon nanotubes were added to the willow catkins solution. The mixed solution was sonicated with a pen-type ultrasonic (FS-250N, 105W) for 2 h and then a bath-type ultrasonic (Bransonic M2800H-C, 110W) for another 2 h. The willow catkin-CNT composites films can be obtained by vacuum filtration.

Preparation of dopant solutions:

The n-type dopants (N-DMBI, PEI, DETA) with different weights (100 mg, 300 mg, 500 mg, 700 mg) were dissolved in 9.1 mL dimethylsulfoxide (DMSO) to make different concentration n-type dopant solutions. The obtained solutions were sonicated for 30 min to make them homogeneous before use.

Preparation of n-type willow catkin–CNT composites films：

The willow catkin–CNT composite films were cut into strips of 15 mm in length and 4 mm in width. The n-type dopant solution of 20 μL (prepared above) was dropped onto a strip of the TE film, which would be sucked into the film. Then the wet film was kept in the air for 2h before it was thoroughly washed with deionizing water to remove the excess dopant. After that, the n-type doped film was dried in a vacuum oven for 2h at 60 ^{o}C.

Preparation of compressed willow catkin–CNT composites films：

The willow catkin–CNT composite films were cut into strips of 15 mm in length and 4 mm in width. A strip composite film was sandwiched between two pieces of polyethylene terephthalate (PET) films and then placed on a tablet press (YLJ-24T, HEFEI KEJING). A pressure of 2 MPa was applied and held for a certain period of time (2-20 min). Finally, the compressed TE film was peeled off from the PET films before use.

Preparation of willow catkin–CNT composites films treated with trimethoxyoctadecylsilane (TMOS)：

TMOS was dissolved in methylene chloride (CH2Cl2) with different weights to get different concentration solutions (0.1wt.%, 0.2wt.% and 0.4 wt.%). The TMOS solution was dropped onto the composite films and dried under vacuum at 60 ^{o}C for 1h**.**

The calculation method:

The numerical simulation has been conducted using COMSOL Multiphysics 5.6, which was used to evaluate the temperature distribution on the thermoelectric leg at different hot side temperatures. The heat transfer in solids was chosen as the analysis element. Before calculation, the boundary condition of ambient temperature was set at 25 ^{o}C. The hot side temperatures of thermoelectric legs are set to 35 ^{o}C, 45 ^{o}C, 55 ^{o}C, 65 ^{o}C, 75 ^{o}C and 85 ^{o}C, respectively. The convection heat transfer and the radiation heat transfer are considered in the simulation. The temperature difference of thermoelectric leg with the different thermal conductivities (10 W/m-K, 50 W/m-K, 70 W/m-K, 90 W/m-K, 130 W/m-K, 190 W/m-K), width (2 mm, 4 mm, 5 mm, 6 mm, 10mm) and length (30 mm, 50 mm, 70 mm) of thermoelectric legs were simulated by COMSOL multiphysics simulations. In the post-processing process, the steady-state temperature distribution on the surface of the device was obtained, and then we extracted the temperature curve of the central axis of the thermoelectric leg. The temperature difference of thermoelectric leg witahe width of 4mm and

a length of 35mm, with the different thermal conductivities (10.38 W/m-K, 35.31 W/m-K, 50.86 W/m-K) were simulated by COMSOL multiphysics simulations in the same method as above.

Measurements

The electrical conductivity and Seebeck coefficient were measured by SBA-458, NETZSCH, Germany. The thermal conductivity was measured by LFA-467, NETZSCH, Germany. The output voltage and output power of the thermoelectric device were measured by Keithley 2400. Scanning electron microscope images were obtained with a field emission scanning electron microscopy, QUANTA FEG 250. The Raman spectra were measured by Laser Raman Spectrometer. Fourier Transform Infrared spectra (FTIR) were recorded within the wavenumber range of 600−4000 cm^{-1} through Thermo Fisher, Nicolet 6700. Thermogravimetric analysis (TGA) was performed using NETZSCH TG 290 F3 in a nitrogen atmosphere at a heating rate of 10K/min.

Three different samples were prepared to test the electrical conductivity and Seebeck coefficient respectively. The error bar (E) was calculated according to the following equation:

$$E = [\sum_{i=1}^{n} (X_i - X_m)^2 / n]^{0.5} \quad (1)$$

And

$$X_m = \sum_{i=1}^{n} X_i / n \quad (2)$$

Where X_i and n are experimental data and the number of samples, respectively.

Note 1: equation (1)

The normalized areal output power density (^{AP_n}) is used to compare the maximum output power ($^{P_{max}}$) under the same $^{\Delta T}$ conditions, which has been reported in the literature.[2] Detailed explanation is shown as follows:

Assuming the thermoelectric properties of the materials are independent of the temperature, when the temperature difference between the two sides of a TEG is $^{\Delta T}$, the open-circuit voltage (^{E}) is

$$E = (S_p - S_n)\Delta T \tag{3}$$

where ^{S_p} and ^{S_n} are the Seebeck coefficient of a p- and an n-type leg, respectively. The actual output voltage (^{U} of the TE device is

$$U = (S_p - S_n)\Delta T \frac{R_L}{R_{in} + R_L} \tag{4}$$

where $^{R_{in}}$ is the internal resistance of the TEG and ^{R_L} is the load resistance. The current (^{I}) in the circuit is

$$I = \frac{(S_p - S_n)\Delta T}{R_{in} + R_L} \tag{5}$$

Therefore, the output power (^{P}) of the TE device is

$$P = \frac{(S_p - S_n)^2 \Delta T^2 R_L}{(R_{in} + R_L)^2} \tag{6}$$

The maximum output power ($^{P_{max}}$) will be obtained when the load resistance ^{R_L} equals the internal resistance $^{R_{in}}$ as shown in equation (7):

$$P_{max} = \frac{(S_p - S_n)^2 \Delta T^2 R_{in}}{(2R_{in})^2} = \frac{(S_p - S_n)^2 \Delta T^2}{4R_{in}} \tag{7}$$

To get the ^{AP_n}, the internal resistance of the device is the sum of the

resistance of the p- and n-type legs by assuming that the contact resistance between the electrodes and the p/n legs is negligible. The internal resistance R_{in} of the device is

$$R_{in} = N(1/\sigma_p + 1/\sigma_n)\frac{l_{leg}}{A_{leg}} \quad (8)$$

where A_{leg} is the contact area between the heat source and the TEG leg assuming the p- and n-type legs have the same dimension. N is the number of p/n type lelegsThen, equation (7) can be re-written as:

$$P_{max} = N\frac{(S_p - S_n)^2 \Delta T^2 A_{leg}}{4(1/\sigma_p + 1/\sigma_n)l_{leg}} \quad (9)$$

The normalized areal output power density AP_n is defined as the P_{max} divided by the contact area (A) between the heat source and the TEG legs and the ΔT^2 as shown in equation (10).

$$AP_n = \frac{P_{max}}{A * \Delta T^2} = \frac{(S_p - S_n)^2}{4(1/\sigma_p + 1/\sigma_n)l_{leg}} \quad (10)$$

Note 2: parallel model

In the willow catkin-$CNT_{33.3}$ composite system, willow catkin is an insulating polymer and carbon nanotubes are the conductive parts. According to the parallel model,

$$\sigma_{composite} = \sigma_{CNT}\nu + \sigma_W(1-\nu) \quad (11)$$

$$S_{composite} = \frac{S_{CNT}\sigma_{CNT}\nu + S_W\sigma_W(1-\nu)}{\sigma_{CNT}\nu + \sigma_W(1-\nu)} \quad (12)$$

where $\sigma_{composite}$ and $S_{composite}$ are the effective electrical conductivity and Seebeck coefficient of the composite, respectively. σ_{CNT} and S_{CNT} are the

electrical conductivity and Seebeck coefficient of the CNT, respectively. σ_W and S_W are the electrical conductivity and Seebeck coefficient of the willow catkin, respectively. ν is the volume fraction of the CNT. The electrical conductivity of willow catkin is negligible (σ_W is close to zero). Therefore, the above equations (10) and (11) can be simplified as:

$$\sigma_{composite} = \sigma_{CNT}\nu \quad (13)$$

$$S_{composite} = S_{CNT} \quad (14)$$

The simplified equation indicates that the electrical conductivity of willow catkin-CNT composites increases with the CNT volume concentration as well as the weight concentration (wt.%), while the Seebeck coefficient is nearly constant. Similar results were observed in the previously reported literature.[3, 4]

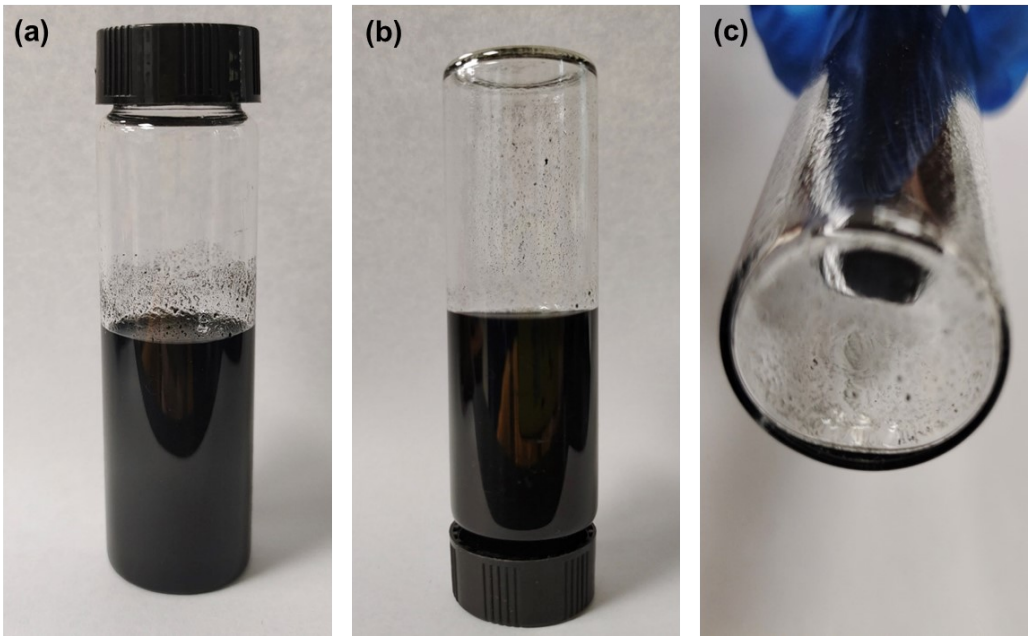

Figure S1 The optical images of willow catkin-XFS16-CNT suspension stored for 10 days.

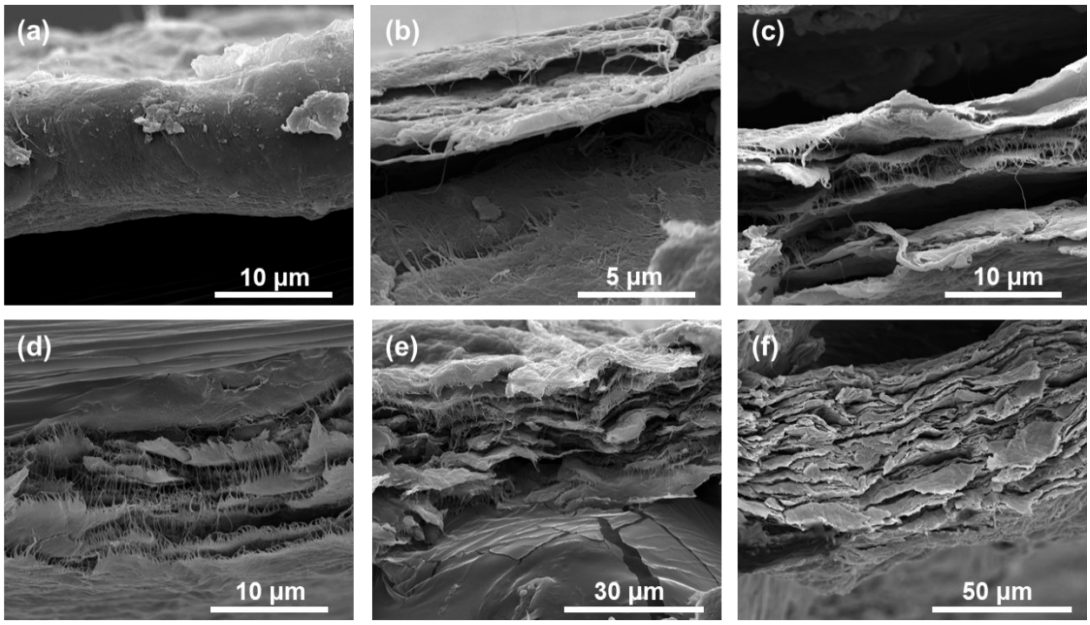

Figure S2 The cross-section of CNT (a), layer-by-layer structure of willow catkin-XFS16-$CNT_{66.7}$ (b), willow catkin-XFS16-$CNT_{33.3}$ (c), willow catkin-XFS16-$CNT_{16.7}$ (d), willow catkin-XFS16-$CNT_{9.1}$ (e), willow catkin-XFS16-$CNT_{3.2}$ (f).

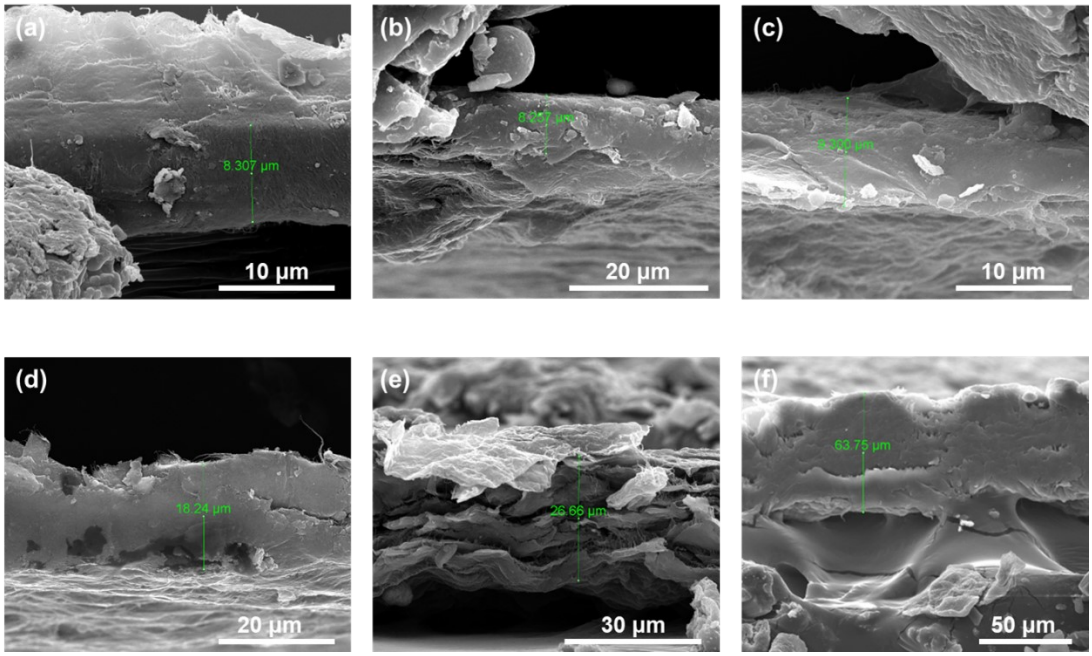

Figure S3 The cross-section of CNT (a), willow catkin-XFS16-$CNT_{66.7}$ (b), willow catkin-XFS16-$CNT_{33.3}$ (c), willow catkin-XFS16-$CNT_{16.7}$ (d), willow catkin-XFS16-$CNT_{9.1}$ (e), willow catkin-XFS16-$CNT_{3.2}$ (f).

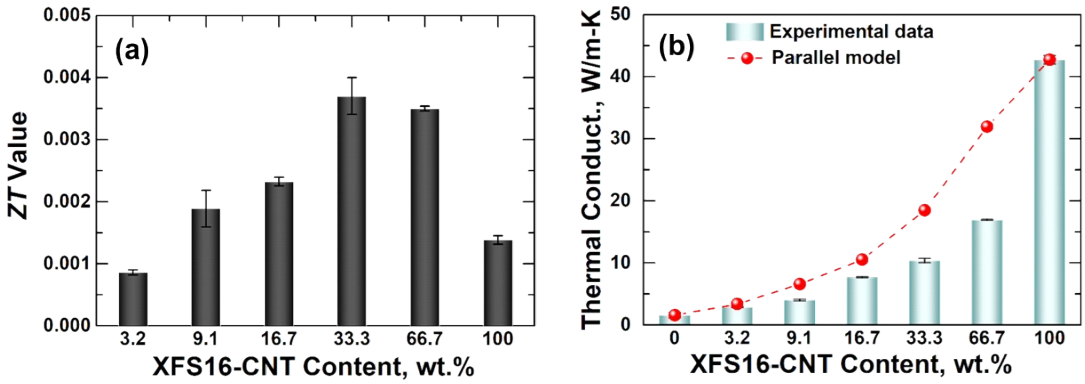

Figure S4 The *ZT* value (a) and thermal conductivity (b) of composites as a function of XFS16-CNT concentrations.

Thermal conductivity was tested to fully evaluate the thermoelectric performance of the willow catkin-XFS16-CNT composites (**Figure S4**). The thermal conductivities discussed in this work were all in-plane thermal conductivities measured by the laser flash method. The thermal conductivity of the original willow catkin film was 1.57 W/m-K, which is higher than the typical thermal conductivities for amorphous polymers.[5] At low CNT concentration, the thermal conductivity of willow catkin-CNT composite did not increase much, e.g. 2.88 W/m-K for willow catkin-XFS16-$CNT_{3.2}$, 4.03 W/m-K for willow catkin-XFS16-$CNT_{9.1}$. When the CNT concentration was 66.7 wt.%, the thermal conductivity of willow catkin-XFS16-$CNT_{66.7}$ reached up to 16.93 W/m-K, which was only two-fifth of the thermal conductivity of CNT-only film. The thermal conductivities of the willow catkin-XFS16-CNT composites were calculated by a parallel model according to the thermal conductivity of each component. The equation of the thermal conductivity calculation with the parallel model is shown below without considering the phonon scattering and size effects.[6]

$$\kappa_{composites} = \kappa_1(1-\nu) + \kappa_2\nu \quad (4)$$

where κ_1 is the thermal conductivity of the continuous phase, κ_2 is the thermal conductivity of the dispersed phase. The calculated values showed the same trend as the experimental results that the thermal conductivity of willow catkin-

XFS16-CNT composite increases with the increase of CNT concentration (**Figure S4b**). However, the calculated value was obviously larger than the experimentally measured thermal conductivity. This indicated that the phonon scattering effects in the willow catkin belts and CNT bio-composites would play an important role in reducing the thermal conductivity of the willow catkin-XFS16-CNT composites. The phonon scattering effects may be caused by the layer-by-layer structure in the bio-composites as shown in the SEM image of the cross-section of willow catkin-XFS16-$CNT_{33.3}$ (**Figure S2**). The layered structure can effectively scatter phonons to reduce the thermal conductivity of TE materials as reported in previous literature.[7-9] *ZT* values of the composites and the CNT-only film were shown in **Figure S4a**. Because of the lower thermal conductivity, *ZT* values of the composites are higher than that of the CNT-only film (0.0014), starting from the CNT concentration of 9.1 wt.%. Among them, willow catkin-XFS16-$CNT_{33.3}$ shows the highest *ZT* of 0.0037, which is ~3 times higher than that of the CNT-only film.

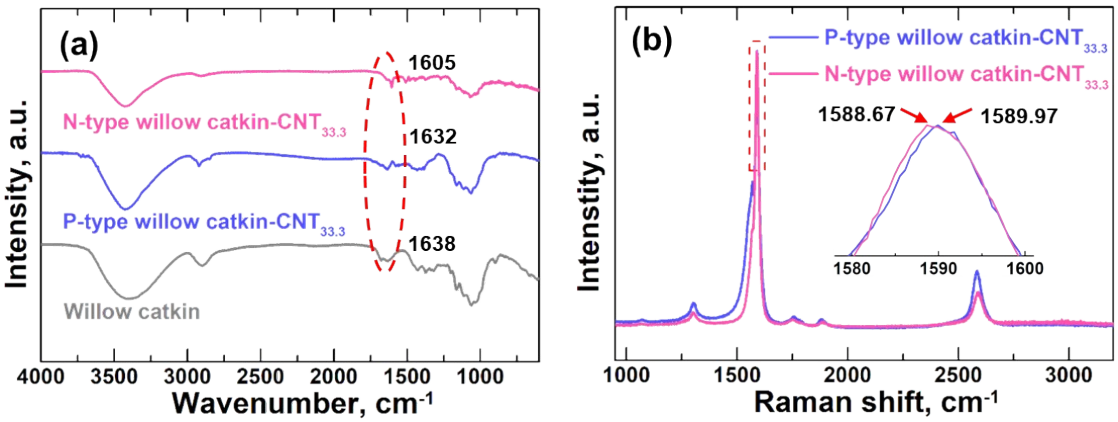

Figure S5 FTIR spectrum of willow catkin, willow catkin-XFS16-$CNT_{33.3}$ and N-DMBI doped willow catkin-XFS16-$CNT_{33.3}$ (a) and Raman spectrum of willow catkin-XFS16-$CNT_{33.3}$ and N-DMBI doped willow catkin-XFS16-$CNT_{33.3}$ (b).

The p- to n-type conversion of the N-DMBI doping of willow catkin-XFS16-$CNT_{33.3}$ was identified by FTIR and Raman spectra. **Figure S5a** shows the FTIR spectra of willow catkin, willow catkin-XFS16-$CNT_{33.3}$ before and after N-DMBI doping. There is a peak at 1638 cm^{-1}, which is assigned to C-O stretching in condensed aldehyde of willow catkin.[10] This peak redshifts to 1632 cm^{-1} after willow catkin was mixed with CNT, indicating the strong interaction between CNT and willow catkin.[11] The addition of N-DMBI will further move this peak to 1605 cm^{-1}. N-DMBI can also increase the conjugation of CNTs by reducing the carbonyl groups or C-O groups on the surface of CNT, which is identified by the reduction of the ratio of the intensity of defect band/graphitic band (I_D/I_G) in N-DMBI doped willow catkin-XFS16-$CNT_{33.3}$ film as compared to that in original willow catkin-XFS16-$CNT_{33.3}$ (**Figure S5b**). A slight redshift has also been observed in the Raman spectra of N-DMBI doped willow catkin-$CNT_{33.3}$ compared to that of original willow catkin-XFS16-$CNT_{33.3}$ (inserted image in **Figure S5b**), which is typical for n-type doping CNTs.[12]

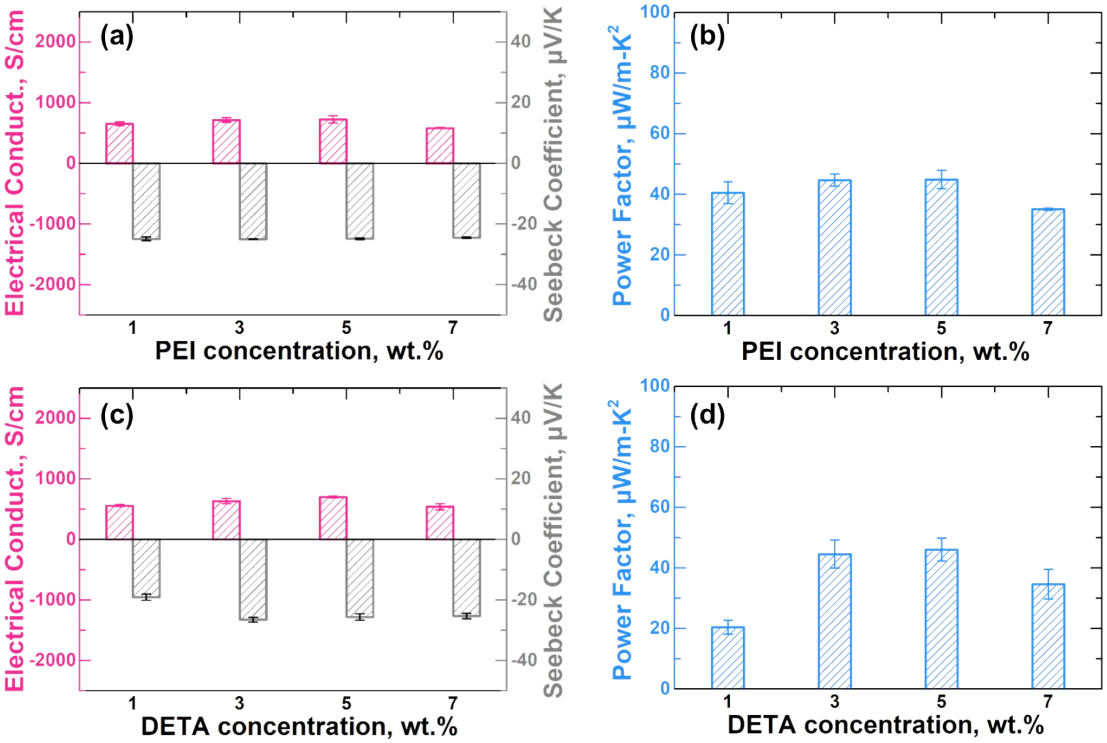

Figure S6 The electrical conductivity and Seebeck coefficient (a) and power factor (b) of willow catkin-XFS16-$CNT_{33.3}$ as a function of the concentration of PEI; the electrical conductivity and Seebeck coefficient (c) and power factor (d) of willow catkin-XFS16-$CNT_{33.3}$ as a function of the concentration of DETA.

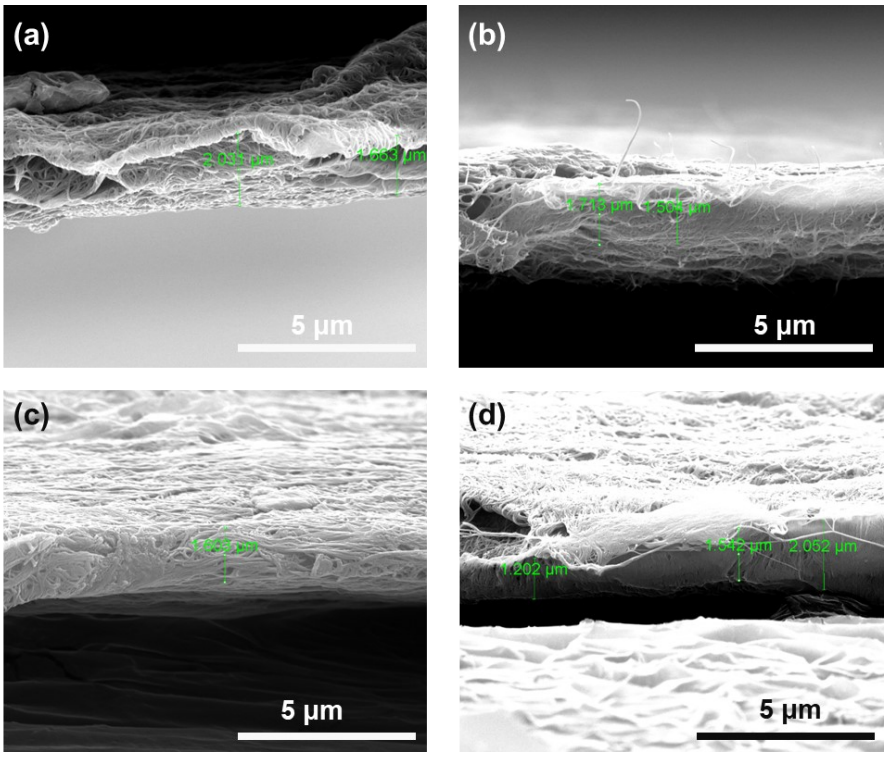

Figure S7 SEM images of the cross-section of p-type cold-pressed willow catkin-XFS16-$CNT_{33.3}$ (a), n-type cold-pressed willow catkin-XFS16-$CNT_{33.3}$/N-DMBI (b), p-type cold-pressed willow catkin-XFS22-$CNT_{33.3}$ (c) and n-type cold-pressed willow catkin-XFS22-$CNT_{33.3}$/N-DMBI (d).

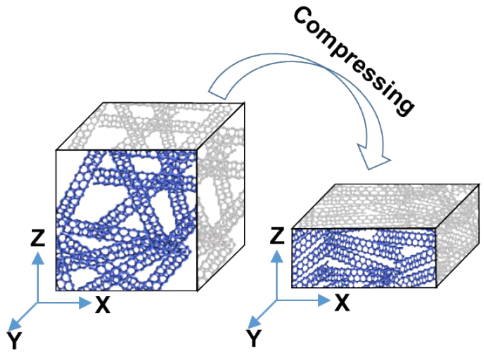

Figure S8 illustration of the change of the concentration of CNT at the xz-plane after compressing.

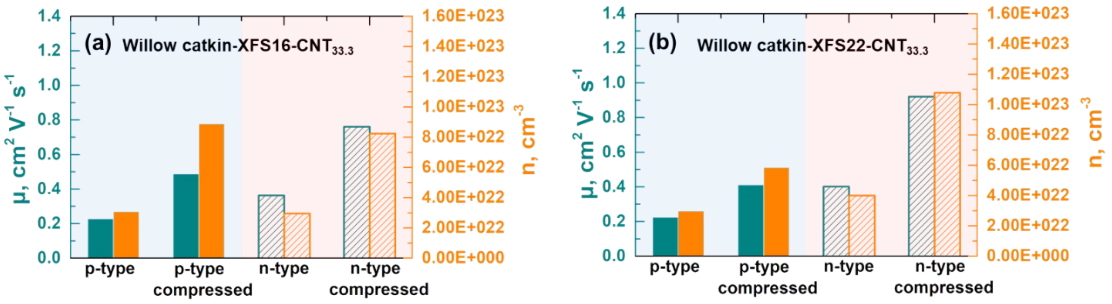

Figure S9 The carrier mobility (μ) and carrier concentration (n) of willow catkin-XFS16-$CNT_{33.3}$ (a) and willow catkin-XFS22-$CNT_{33.3}$ (b) before and after compressed.

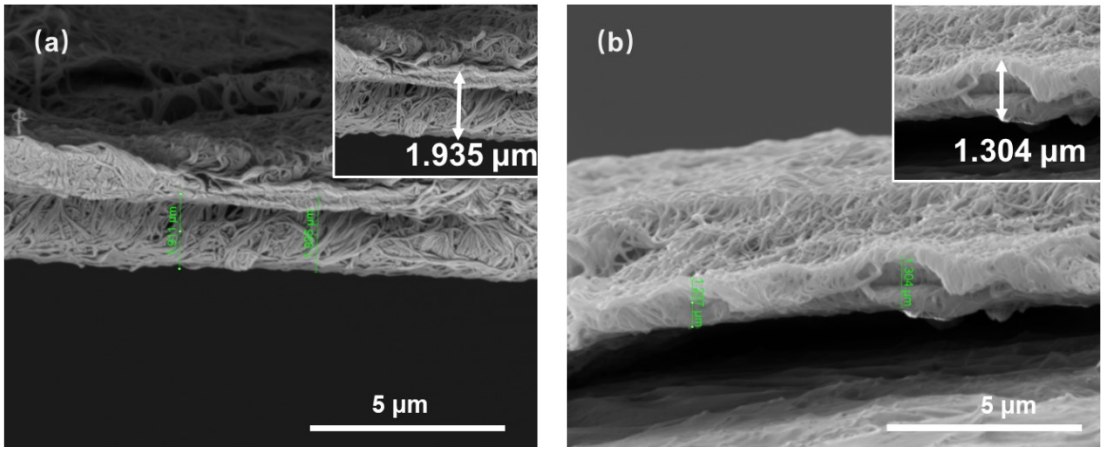

Figure S10 SEM images of the cross-section of compressed p-type willow catkin-XFS22-$CNT_{33.3}$ (a) and compressed n-type willow catkin-XFS22-$CNT_{33.3}$/N-DMBI (b) films after releasing the pressure and being exposed to the air for 7 days.

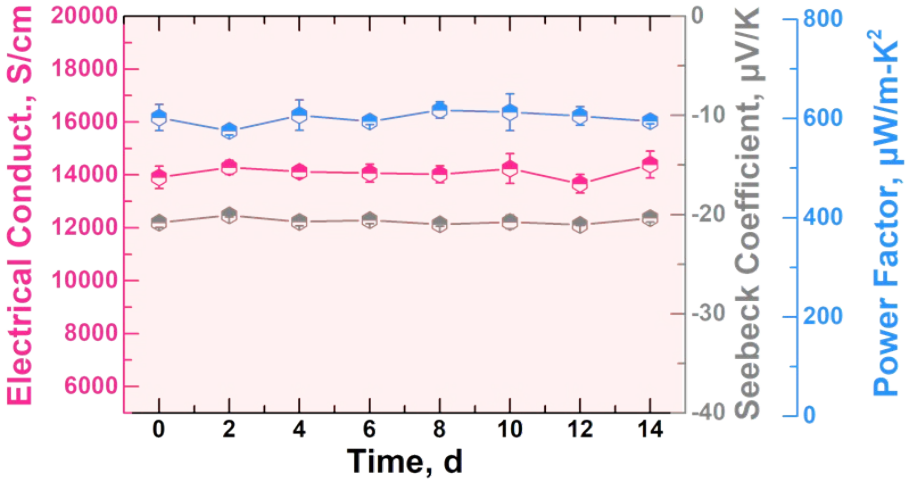

Figure S11 The electrical conductivity, the Seebeck coefficient and the power factor of the compressed n-type willow catkin-XFS22-$CNT_{33.3}$/N-DMBI film as a function of the time when the film was exposed in the air.

The compressed n-type willow catkin-XFS22-$CNT_{33.3}$/N-DMBI also exhibited good air stability as shown in **Figure S11**. The electrical conductivity and Seebeck coefficients were nearly constant after the film being exposed to the air for 14 days. The good air stability of the n-type SWCNT films was attributed to the good stability of the n-type dopant N-DMBI as well as the good coverage of the dopant molecules on CNTs which prevented the oxidation of CNTs by oxygen, thus leading to stable electrical conductivity and Seebeck coefficient of the films in the air. Similar results were also reported in the literature that N-DMBI doped n-type CNTs could have stable electrical properties in the air.[13, 14]

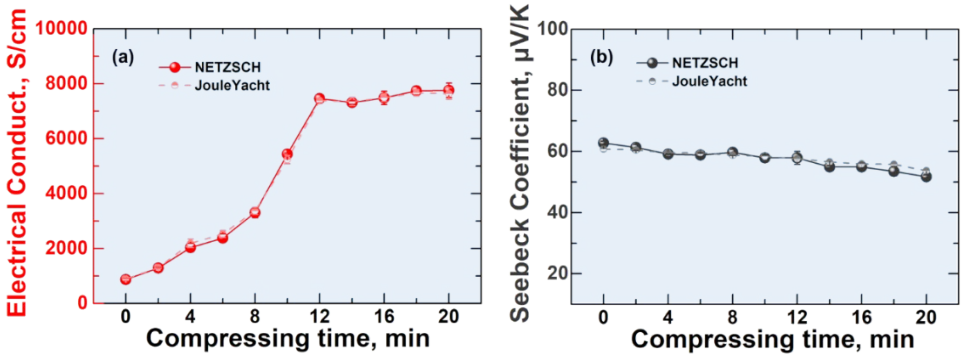

Figure S12 The electrical conductivity and Seebeck coefficient of compressed p-type willow catkin-XFS22-$CNT_{33.3}$ measured by two instruments.

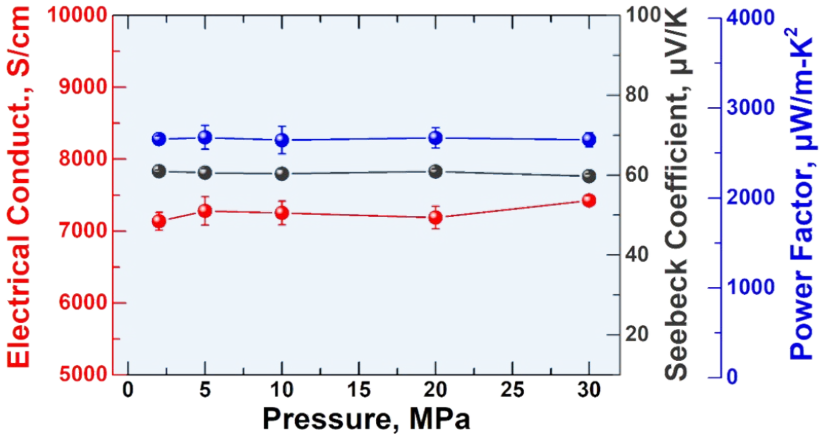

Figure S13 The thermoelectric properties of p-type willow catkin-XFS22-$CNT_{33.3}$ as a function of the pressure.

Figure S13 showed that the electrical conductivity, the Seebeck coefficient and the power factor of the p-type willow catkin-XFS22-$CNT_{33.3}$ film as a function of the pressure. The electrical properties of the p-type willow catkin-XFS22-$CNT_{33.3}$ film were nearly constant when the film was compressed for 12 min in the pressure range of 2-30 MPa. The results indicated that the pressure of 2 MPa was high enough and increasing the pressure would not make the film denser. In the meanwhile, the pressure was much lower than the pressure value that could make the CNT cylinder deform, which was about several GPa [15-17].

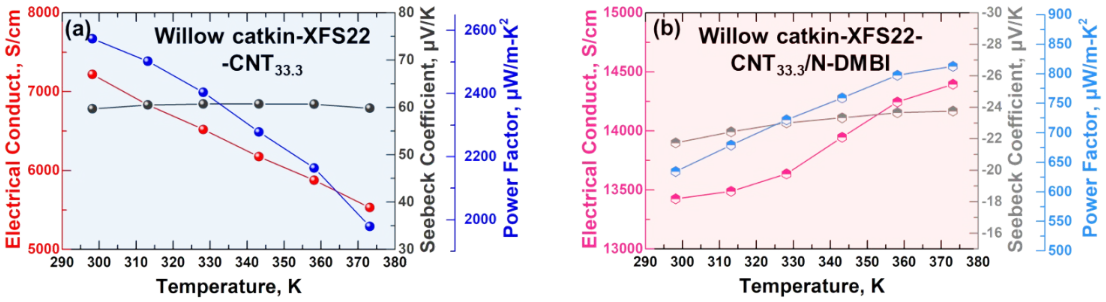

Figure S14 The temperature dependence of thermoelectric properties of compressed p-type willow catkin-XFS22-CNT33.3 (a) and compressed n-type willow catkin-XFS22-CNT33.3/N-DMBI (b).

The electrical conductivity decreased and the Seebeck coefficient was maintained for the compressed p-type film when increasing the temperature from 298 to 373 K. While the electrical conductivity increased and the Seebeck coefficient was nearly constant for the compressed n-type film when increasing the temperature in the same range. The results were consistent with the trends for previously reported p- and n-type CNT composite films, respectively[12, 18-21].

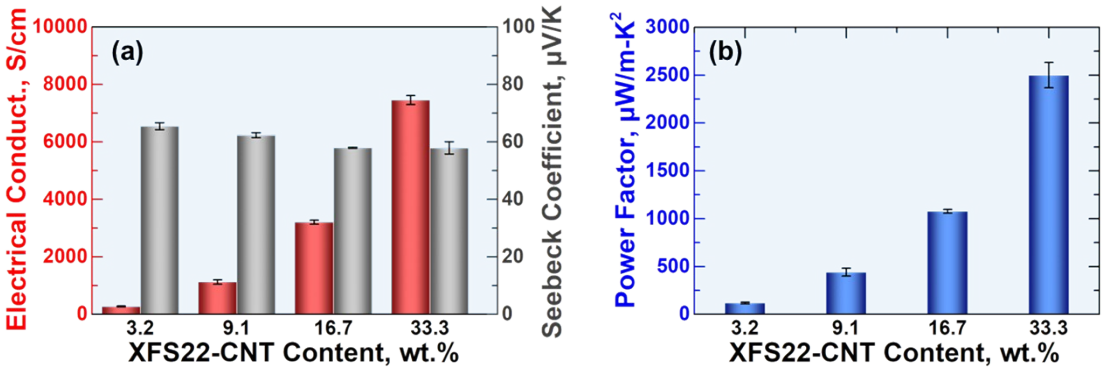

Figure S15 The electrical conductivity and Seebeck coefficient (a), power factor (b) of compressed willow catkin-XFS22-CNT composites as a function of XFS22-CNT concentrations.

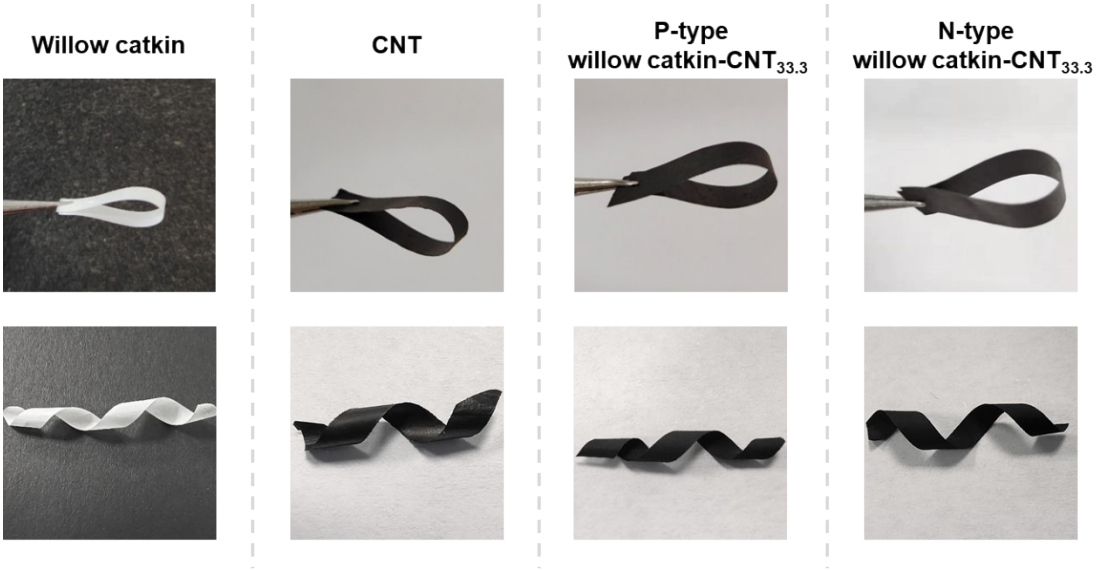

Figure S16 Optical image of bent willow catkin films, XFS22-CNT films, p-type and n-type cold-pressed willow catkin-XFS22-CNT films.

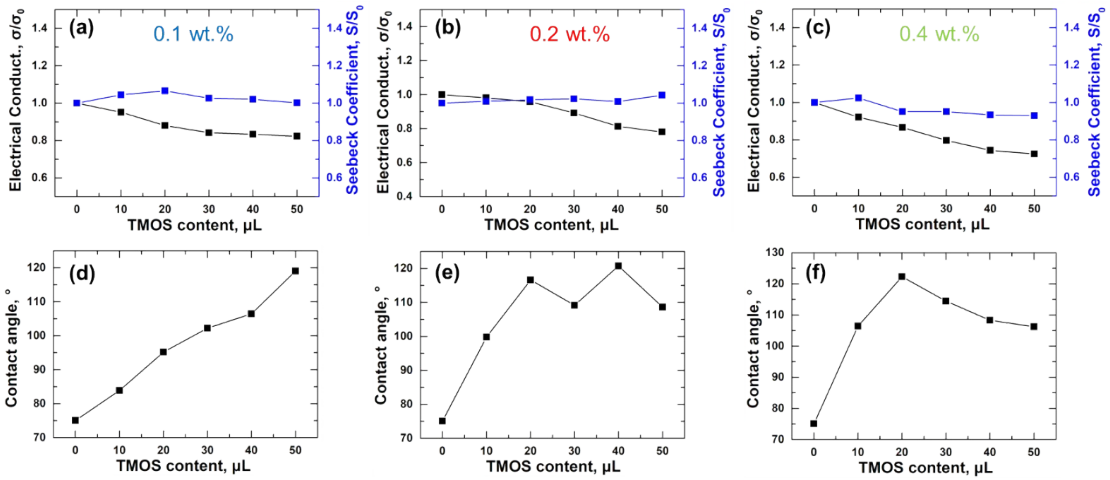

Figure S17 The thermoelectric properties and contact angle of willow catkin-$CNT_{33.3}$ films treated by trimethoxyoctadecylsilane.

In order to obtain the willow catkin-CNT films with hydrophobic properties, the willow catkin-$CNT_{33.3}$ film was treated with different concentrations of trimethoxyoctadecylsilane (TMOS). **Figure S17** shows the thermoelectric properties and contact angle of 33.3% CNT/catkin willows composites coated by 0.1 wt.%, 0.2 wt.% and 0.4 wt.% octadecyltrimethoxysilane. The sample treated with 0.1 wt.% octadecyltrimethoxysilane showed a maximum contact angle of 119° and maintained 82 % of its electrical conductivity and Seebeck coefficient did not change. The sample treated with 0.2 wt.% octadecyltrimethoxysilane showed a maximum contact angle of 121° and maintained 90 % of its electrical conductivity and 98 % of its Seebeck coefficient. The sample treated with 0.4 wt.% octadecyltrimethoxysilane showed a maximum contact angle of 122° and maintained 72 % of its electrical conductivity and 93 % of its Seebeck coefficient.

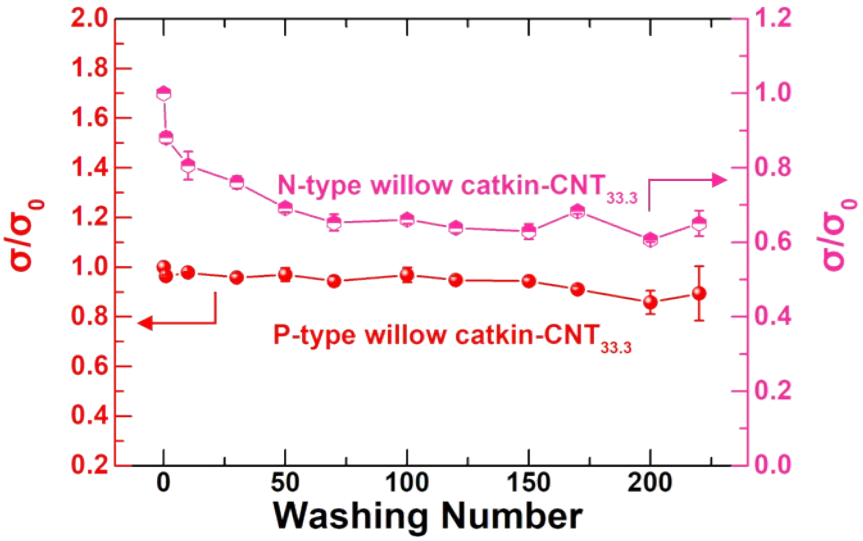

Figure S18 The electrical conductivities of the compressed p- and n-type willow catkin-XFS22-$CNT_{33.3}$ after 220 times of washing cycles.

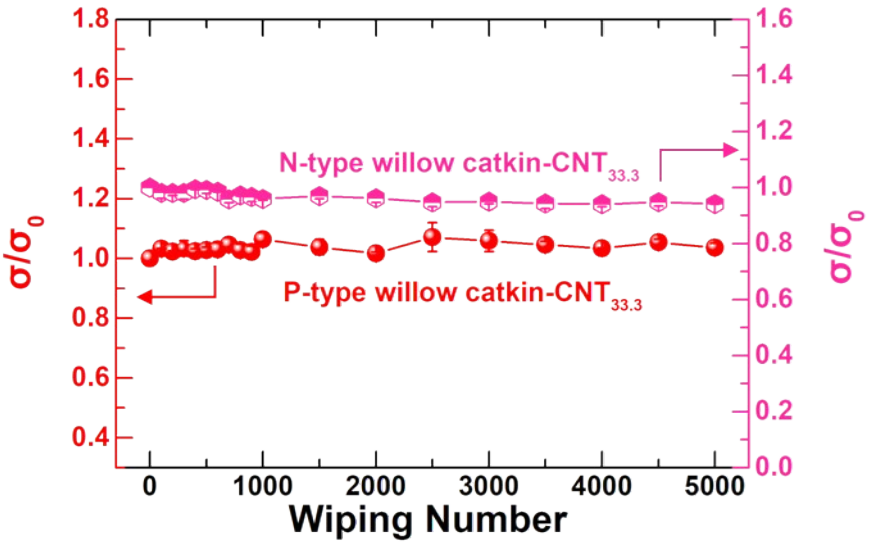

Figure S19 The electrical conductivities of the compressed p- and n-type willow catkin-XFS22-$CNT_{33.3}$ after 5000 times of wiping.

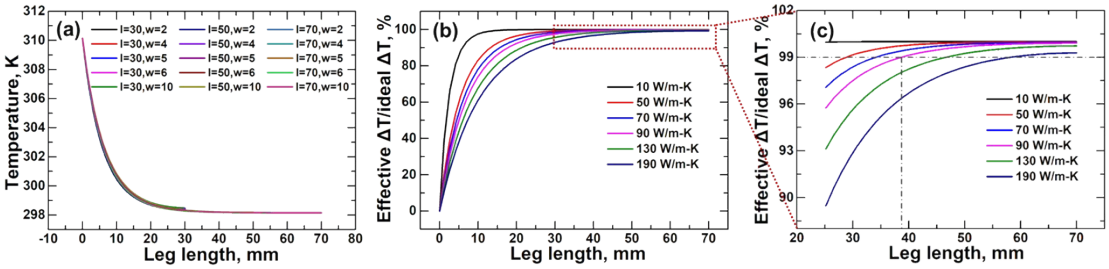

Figure S20 Effective temperature difference efficiency of the TEG legs as a function of the distance from a hot-side temperature of 358K.

Figure S20a demonstrated that the width had little effect on the temperature gradient for a film with thermal conductivity of 50 W/m-K. The temperature matched each other when the width varied in the range of 2-10 mm for the samples with different lengths of 30, 50, and 70 mm. **Figure S20b** showed that temperature gradient along the length of TEG legs (Effective $^{\Delta T}$) with a width of 4 mm and different thermal conductivities. The results indicated that the effective $^{\Delta T}$ can be 99% of the ideal $^{\Delta T}$ when the length of the TEG legs was ~40 mm and the TEG legs had a thermal conductivity < 90 W/m-K.

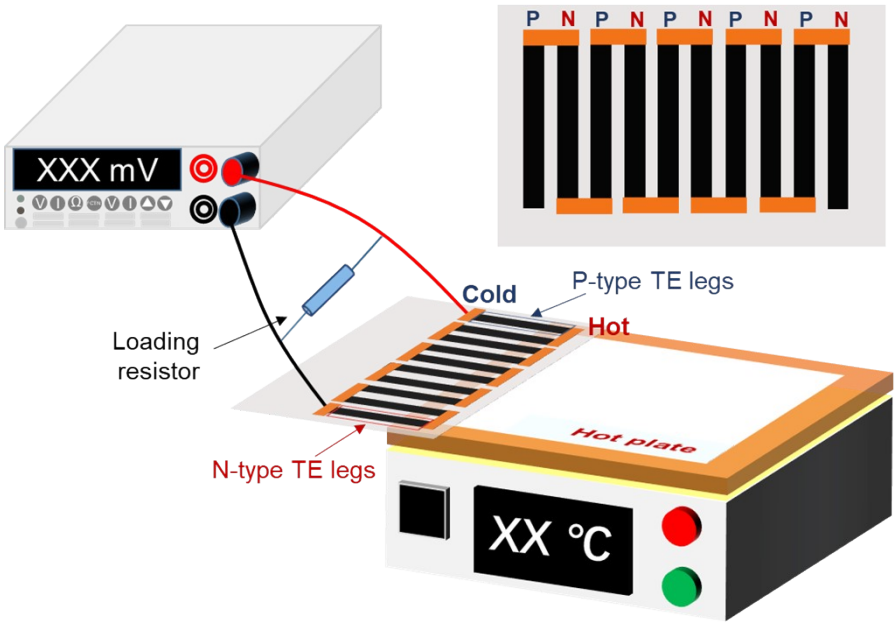

Figure S21 Schematic diagram of thermoelectric device testing.

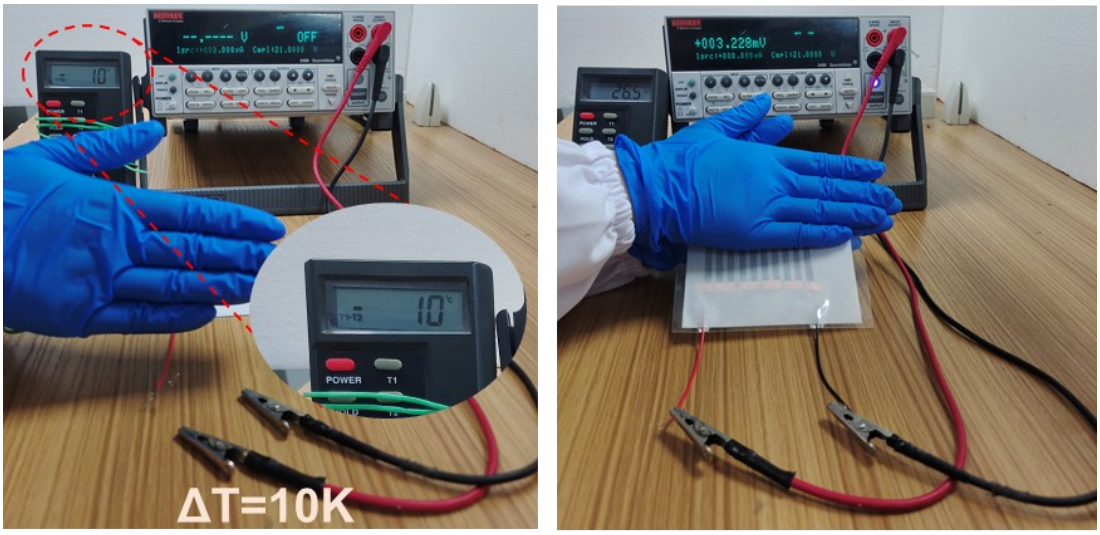

Figure S22 Output voltage of the original fabricated TEGs at a temperature gradient of ~10 K generated by human hands after over 240 days in the glovebox.

The originally fabricated TEG exhibited great stability under N_2 protection in the glovebox as shown in **Figure S22**. It could still generate 3.2 mV thermoelectric voltage when held with human hands at a temperature gradient of ~10 K after being stored in the glovebox for over 240 days. The obtained thermoelectric voltage matched well with that generated by the as-prepared device (3.4 mV) as shown in **Figure 6d**.

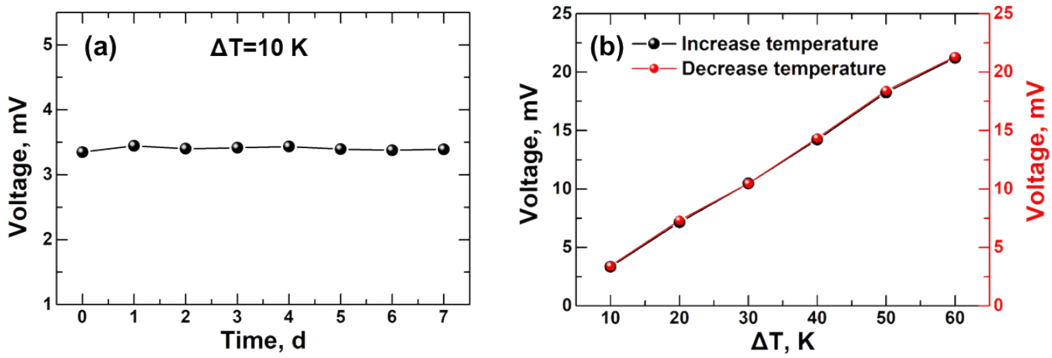

Figure S23 The air stability (a) and thermal conductivity (b) of TEG-XFS22/compressed.

The generated thermoelectric voltage of 3.3 mV for the TE device was almost constant at the temperature gradient of 10 K with the cold side temperature of 298 K (room temperature) when the device was exposed to the air for 7 days (**Figure S23a**). When increasing the temperature gradient from 10 K to 60 K, the generated thermoelectric voltage became 21.2 mV. When reversely tuning the temperature gradient, the generated thermoelectric voltage values matched well with that obtained in the temperature gradient increasing process (**Figure S23b**). The results indicated that the fabricated device had good thermal stability in the temperature range of 298 K- 358 K in the air.

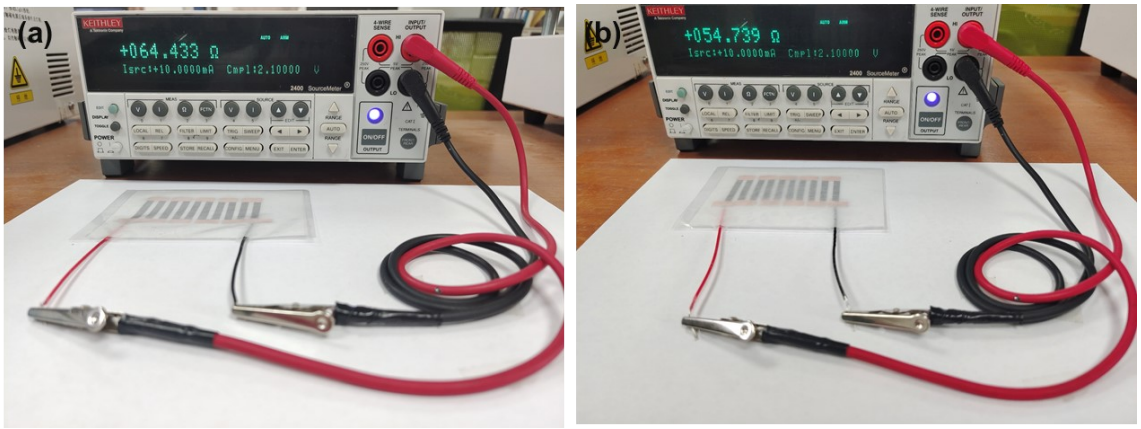

Figure S24 The internal resistance of TEG-XFS16/non-compressed (a) and TEG-XFS16/ compressed (b).

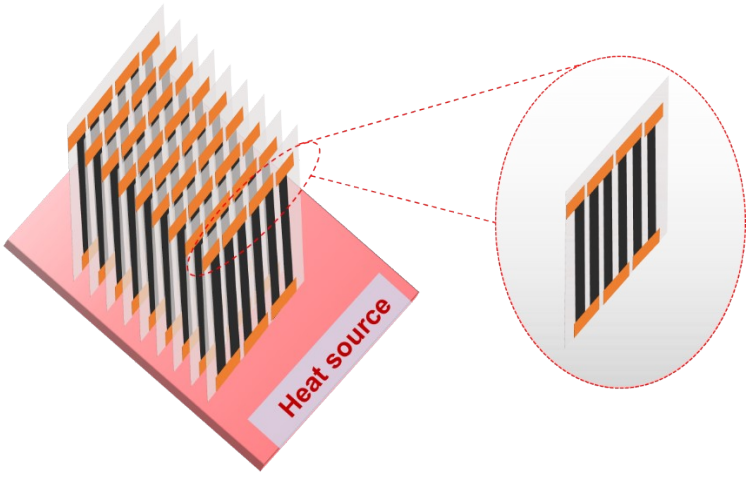

Figure S25 Schematic diagram of the integration of the TEGs on a heat source.

Typically, the output power of a TEG could be infinite if the area of the heat source is infinite. The power density is important since the area of a heat source in practice is limited. Therefore, the maximum area output power density is typically defined as the maximum output power divided by the contact area between the TEG and the heat source in the literature.[22-24] The TEG legs were perpendicular to the surface of the heat source. $^{AP}{}_{max}$ was calculated by dividing the $^{P}{}_{max}$ with the sum of the cross-section area of all the legs.

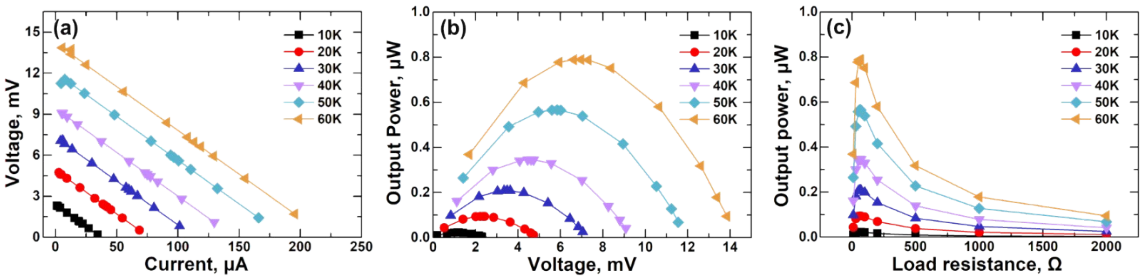

Figure S26 The voltage-current curve of TEG-XFS16/non-compressed at different temperature gradients (a); the output power-voltage curve of TEG-XFS16/non-compressed (b); the output power of the TEG-XFS16/non-compressed as a function of load resistance (c).

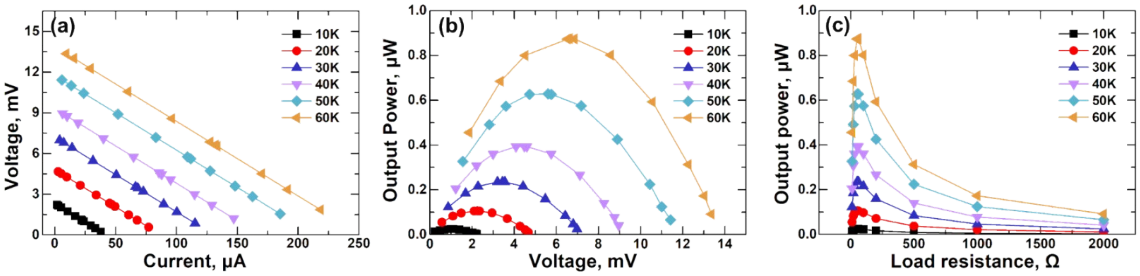

Figure S27 The voltage-current curve of TEG-XFS16/pressed at different temperature gradients (a); the output power-voltage curve of TEG-XFS16/pressed (b); the output power of the TEG-XFS16/pressed as a function of load resistance (c).

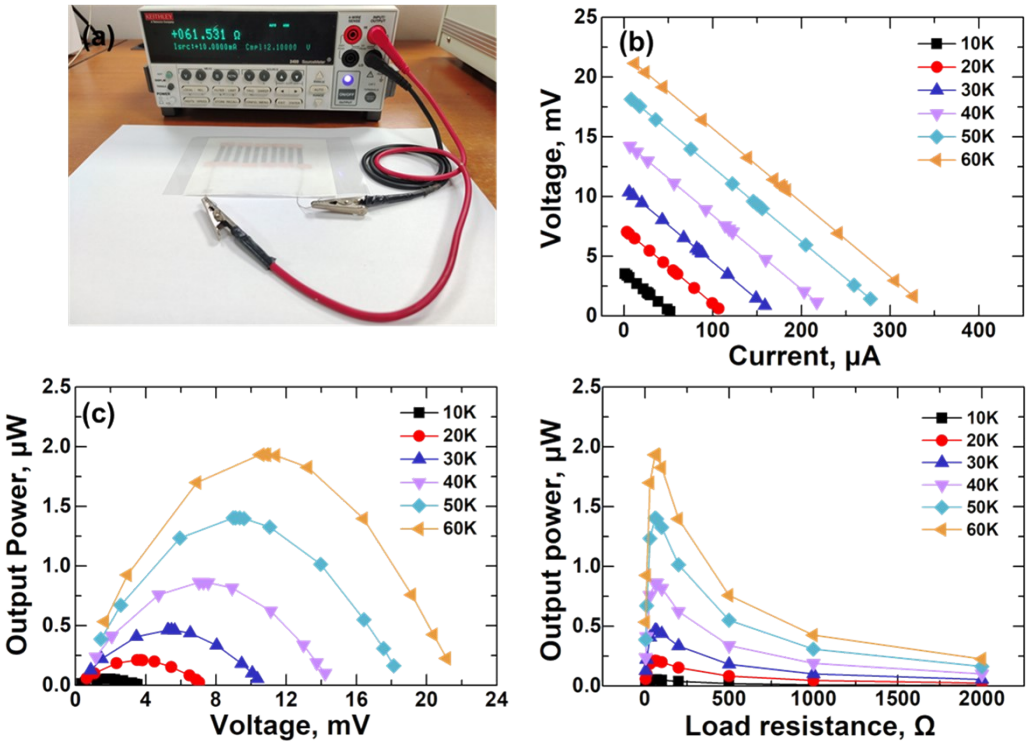

Figure S28 The internal resistance of TEG-XFS22/non-compressed (a); the voltage-current curve of TEG-XFS22/non-compressed at different temperature gradients (b); the output power-voltage curve of TEG-XFS22/non-compressed (c); the output power of the TEG-XFS22/non-compressed as a function of load resistance (d).

A new TE device with 5 pairs of p- and n-type legs was fabricated with non-compressed p-type willow catkin-XFS22-$CNT_{33.3}$ and non-compressed n-type willow catkin-XFS22-CNT33.3/N-DMBI to show the heat-to-electricity conversion ability of TEG-XFS22/non-compressed. **Figure S28a** showed that the internal resistance of TEG-XFS22/non-compressed was ~61.5 Ω. The output voltage and output power of TEG-XFS22/non-compressed were shown in **Figure S28**. TEG-XFS22/non-compressed had an output voltage of 21.9 mV and a P_{max} of 1.9 μW at the temperature gradient of 60 K, which was close to that of the TEG-XFS22/pressed (2.0 μW). However, the TEG-XFS22/pressed required a smaller contact area which would have a higher normalized output power density (AP_n) than TEG-XFS22/non-compressed (**Table S2**).

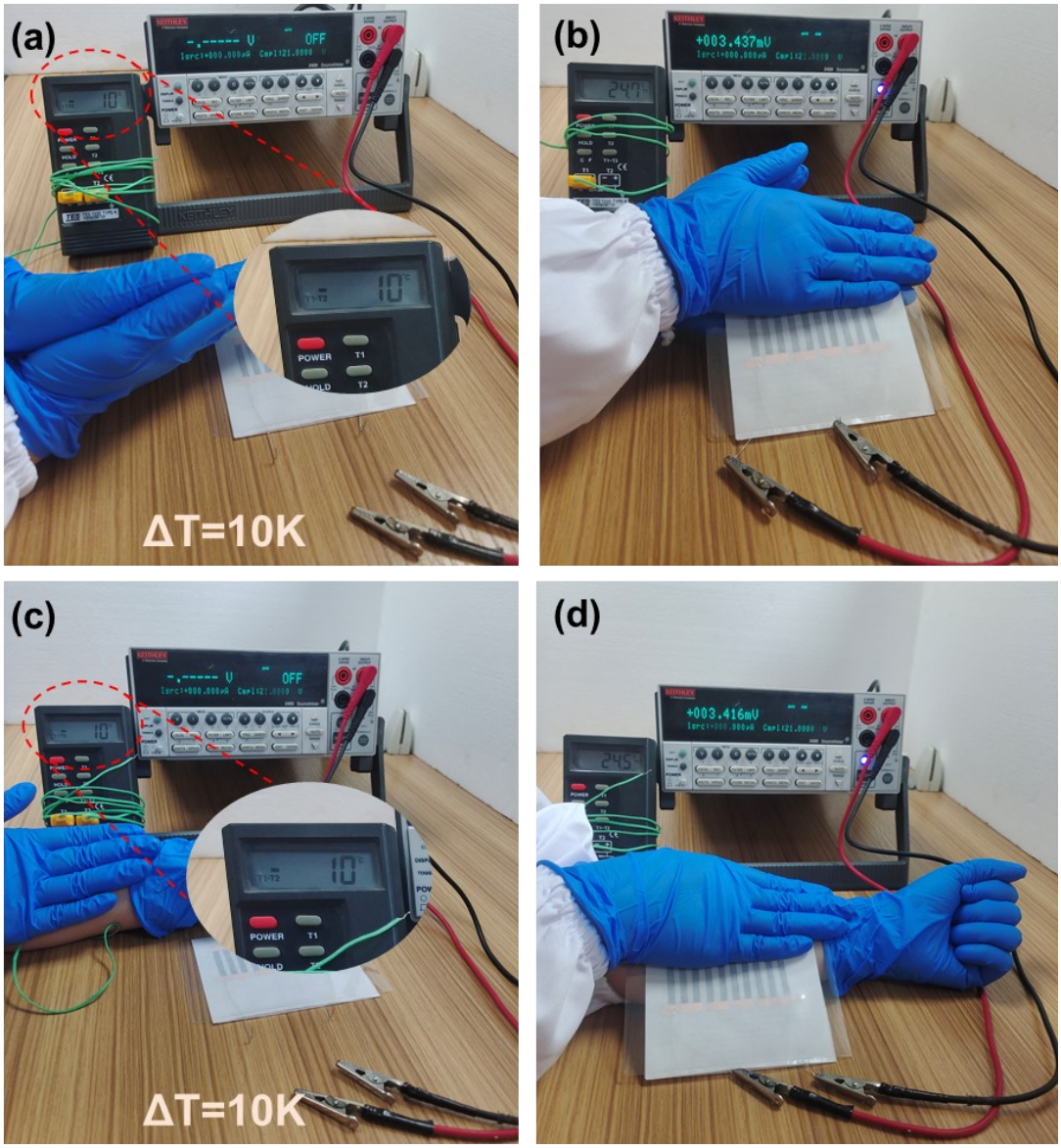

Figure S29 The output voltage of TEG-XFS22/compressed at a temperature gradient of ~10 K generated by human hands (a)-(b) and arms (c)-(d).

The temperature gradient between the human hand/arm and the room temperature was 10 K. The TEG-XFS22/compressed with 5 pairs of p- and n-type legs (35 mm in length, 4 mm in width) could generate a thermoelectric voltage of 3.4 mV as shown in **Figure S29**. In the meanwhile, the TE voltage could be increased while increasing the number of TE legs. The results demonstrated the potential application of flexible TE materials and devices in wearable applications to support low-power devices.

Table S1 Comparison of thermoelectric properties for free-standing polymer-CNT composites with CNT concentration up to >90 wt.%.

Materials	CNT wt.%	σ, S/cm	S, μV/K	PF, μW/m-K^2	Ref.
Compressed p-type willow catkin-XFS22-CNT$_{33.3}$ films	33	7455.8	57.9	2500	This work
Compressed p-type willow catkin-XFS16-CNT$_{33.3}$ films	33	11080.5	32.8	1196	This work
SWCNT/polystyrene	75	2120	61	789	[25]
Compressed n-type willow catkin-XFS22-CNT$_{33.3}$/N-DMBI	33	14871.88	-19.89	588.21	This work
Compressed n-type willow catkin-XFS16-CNT$_{33.3}$/N-DMBI	33	10112.34	-23.29	548.35	This work
CNT/ PEDOT	—	547.2	82.9	504.8	[26]
poly(metaTFSI)/SWCNT	92	1000	70	490	[27]
SWCNT/PVDF	50	2000	43	378	[28]
SWCNT/PANI	73	2355.7	39.2	362	[29]
PEDOT-PF$_6$/SWCNT	80	3600	31.1	350	[30]
PEDOT:PSS/CNTF	—	950	59	330	[24]
OSCs/SWCNT	50	823.9	59.3	304.9	[31]
PPy/a-SWCNT	80	3850	25	240.3	[32]
PANI/DWCNT	30	610	61	220	[33]
SWCNT/ZnTPP	33	926.7	46.9	203.8	[34]
PhC2Cu/SWCNT	90	666.2	55	200.2	[35]
PEDOT:PSS/SWCNT	90	1602.6	33.4	182.7	[36]
P2/SWCNT	50	3283.09	22.4	161.34	[37]
PEDOT:PSS/SWCNT	60	1350	41	160	[38]
PEDOT/CNT	67	679	48	157	[39]
PEDOT:PF$_6$/SWCNT	80	1444.5	32	150	[40]
PEDOT:Tos/SWCNT	35	4731.6	15.9	119.4	[41]
PEDOT:PSS/PVA/SWCNT	60	1800	24	106.1	[42]
Poly(ANi-co-Py)/SWCNT	60	1035.3	28.3	83.2	[43]
AC cotton/GnPs	40	2.2	14	0.04	[44]
SWCNT/FcMA	12.5	2674.86	-46.07	567.54	[45]
SWCNT/PVDF/PEI	50	1950	-37.6	289	[28]
SWCNT/ADLA2	50	529.6	-60.7	195.2	[46]
SWCNT/PYB	8.3	823.05	-48.5	193.6	[47]
SWCNT/CTAB	67	840	-47	185.7	[48]

PEG/NaOH/SWCNT	—	1708.5	-31.9	173.8	[49]
SWCNT/NDINE	50	400	-57	135	[50]
CNT/PEDOT:PSS/PEI	40	289	-45	125	[51]
SWCNT/ADTAb	50	642.4	-44.5	124.4	[52]
C8BTBT–F_4TCNQ/SWCNT	—	520.2	-45	105.1	[53]
dppf@SWNT	85	716	-38	103.4	[54]
SWCNT/ E7	66	530.27	-42.57	95.37	[55]
NDI-1/SWCNT	80	351.4	-47.5	79.6	[56]
SWCNT/cellulose acetate/PEI	90	430	-35	51.6	[57]
CNTs/PEI/DETA-$NaBH_4$	—	38	-86	38	[58]
GNP- SWNT/SDBS/PEI	30	280	-34	33	[59]
SWCNT/DETA–CaH2	—	165	-41	27.7	[60]
P(NDI2OD-T2)/SWCNTs/N-DMBI	45.5	312.5	-30	27.7	[61]
SWCNT/BC/PEI	6	90	-50	22.5	[62]
BC/eDIPS SWCNT	6	83.30	49	20	[62]
CPE–PyrBIm4/SWCNT	50	106	-41	17.8	[63]
Cotton/CNTs/PVP	25	55	-3.2	0.06	[44]

Table S2 The maximum output power (P_{max}), maximum areal output power density (AP_{max}), and normalized areal output power density (AP_n) of thermoelectric devices made of CNT-based composites, organic-inorganic hybrids and inorganic material-based TE films. (**Note**: All the AP_{max} values were calculated by dividing the P_{max} with the sum of the cross-section area of all the legs.)

Materials	CNT wt%	△T, K	TE legs	P_{max}, μW	AP_{max}, W/m^2	AP_n, mW/m^2-K^2	Ref.
β-Ag_2Se	—	60			124	34.4	64
PVP/Ag_2Se	—	29.1	6	4.2	28.8	34	65
SWCNT web	—	20	20	7.1	11.8	29.5	66
CNTYs	—	25	1200	1200	11.7	18.7	67
Ag/Ag_2Se	—	29.6	6	6.1	13.6	15.5	68
$Bi_2Te_{2.8}Se_{0.2}$ film	—	60	5	6.1	41	11.4	69
Sb_2Te_3/SWCNT	—	7.5	160	11.3	0.6	10.5	70
PVDF/Ta_4SiTe_4	—	35.5	4	1.7	13.1	10.4	71
Compressed willow catkin-XFS22-$CNT_{33.3}$ films	33.3	60	10	2.0	34.1	9.5	This work
Ta_4SiTe_4/PVDF/GDY	—	35	8	1.5	9.4	7.7	72
MWCNT	—	60	800	120	27	7.5	73
PEDOT/Ag_2Se/CuAgSe	—	36	11	3.2	8.4	6.5	74
SnTe/PbTe	—	120	64		84	5.8	75
SWCNTs/Sb_2Te_3/ RGO/Bi_2Te_3	—	70	20	23.6	26.2	5.4	8
Sb_2Te_3– /Bi_2Te_3–CNT	—	20	300	159.6	1.9	4.8	76
CNT yarn	—	5	480	4.2	0.1	4.2	77
Compressed willow catkin-XFS16-$CNT_{33.3}$ films	33.3	60	10	0.9	14.6	4.1	This work
GNPs-Te-PEDOT: PSS/ SSWNTs-Te-PEDOT: PSS	—	20	14	0.1	1.5	3.8	78
SWCNT/FcMA	12.5	54.1	10	0.8	10	3.4	45
PEG/NaOH/SWCNT	—	76	10	5.3	17.7	3.1	49
Ag_2Se/Ag/CuAgSe	—	45	6	0.5	5.4	2.7	79
Ag_2Se film	—	30	4	460	2.3	2.6	80
SWCNT/NDINE	50	50	10	3.3	5.5	2.2	50
CNTs-Te-PEDOT:PSS	60	67.8	8	1.3	9.2	2.0	81

SWCNT	—	30	120	2.0	1.7	1.9	[82]
PEDOT-Tos/Te/SWCNTs	—	100	10	16	14.2	1.4	[83]
Non-compressed willow catkin-XFS22-$CNT_{33.3}$ films	33.3	60	10	1.9	4.75	1.3	This work
MWCNT	—	38.9	400	950	1.5	1.0	[84]
Non-compressed willow catkin-XFS16-$CNT_{33.3}$ films	33.3	60	10	0.8	2.0	0.6	This work
SWCNT	50	100	—	461	4.5	0.5	[85]
SWCNT	—	27.5	6	2.5	0.3	0.4	[23]
SWCNT/PYB	8.3	66	10	1.2	1.5	0.4	[47]
SWCNT	20	45	48	1.7	0.2	0.1	[86]
SWCNT/DETA	—	55	28	0.6	0.2	0.1	[60]

Table S3 Comparison of ZT value of CNT-based organic thermoelectric composites.

Sample	CNT wt.%	ZT value	Ref
PANI/SWCNT aerogel	50	0.95	[87]
SWCNT- Ar plasma treated	100	0.4 (700K)	[88]
PEDOT:PSS/CQD	—	0.32	[89]
n-PETT/CNT/PVC	38.5	0.3	[90]
n-PETT/CNT/PVC	38	0.3	[91]
PPy/SWCNT	—	0.203	[92]
PEDOT:PSS/SWCNT	74	0.13	[93]
SWCNT/PANI	64	0.12	[94]
s-SWCNTs	100	0.12	[95]
SWNTs/PEDOT:PSS	60	0.12	[96]
SWCNT/TPP	—	0.078	[97]
CuPcI/SWCNT	60	0.03	[98]
PEDOT/SWCNT/BC film	32	0.028	[99]
PBDTDTffBT/SWCNT	91	0.028	[100]
PEDOT:PSS/SWCNT/Graphene	—	0.021	[101]
Willow catkin/XFS22	33	0.021	This work
MWCNT/PVDF	20	0.02	[102]
ZIF-67/CNT	—	0.02	[103]
CNT/PEDOT:PSS	35	0.02	[104]
MWCNT	—	0.019	[105]
P3HT/SWCNT	8	0.015	[106]
PVP–PVA/CNT	—	0.0134	[107]
PEDOT:PSS/CNT	80	0.01	[108]
MWCNT/PANI	1	0.01	[109]
Willow catkin/XFS16	33	9.8×10^{-3}	This work
SWCNT/TPP	—	9.1×10^{-3}	[110]
Parent SWCNT	100	7×10^{-3}	[111]
$Ni_3(HITP)_2$/SWCNT	30	8.77×10^{-3}	[112]
rGO/SWCNT aerogel	37.5	8.03×10^{-3}	[113]
CNT/PDMS foam	10	6.6×10^{-3}	[114]
CNT/PVAc	20	6×10^{-3}	[3]
Willow catkin/XFS22-N-DMBI	33	4.7×10^{-3}	This work
SWCNT/PNDI2OD-T2	9	4.5×10^{-3}	[115]
Pyrene/SSWCNT	—	4.4×10^{-3}	[116]
SWCNTs-supramolecular 2	81.3	4.2×10^{-3}	[117]
Willow catkin/XFS16-N-DMBI	33	3.7×10^{-3}	This work
PEDOT:PSS/SWCNTs/GQDs	1	3.22×10^{-3}	[118]
SWCNT/KOH/18-crown-6-ether		2×10^{-3}	[111]
SWCNT	—	1.8×10^{-3}	[119]
Carbon Nanotube/Cellulose	90	1.8×10^{-3}	[120]

Acetate			
SWCNT	100	1.7×10^{-3}	88
PTh/MWCNT	80	8.71×10^{-4}	121
SWCNT/Span-80	20	8.4×10^{-4}	122
SWCNT/cellulose	8	7.4×10^{-4}	123
F8BT/SWCNT/$FeCl_3$	60	7.1×10^{-4}	124
PA6/SAN/SWCNT	3	2×10^{-4}	125
PP/B-SWCNT	7.5	1.3×10^{-4}	126

References

1. Y. Wu, M. Sun, X. Wu, T. Shi, H. Chen and H. Wang, *Forests*, 2019, **10**, 749.
2. X. Shi and J. He, *Science*, 2021, **371**, 343-344.
3. C. Yu, Y. S. Kim, D. Kim and J. C. Grunlan, *Nano Lett.*, 2008, **8**, 4428-4432.
4. S. Han, S. Chen and F. Jiao, *Compos. Commun.*, 2021, **28**, 100914.
5. J. Chen, X. Huang, Y. Zhu and P. Jiang, *Adv. Funct. Mater.*, 2017, **27**, 1604754.
6. K. S. Reddy and P. Karthikeyan, *Adv. Mech. Eng.*, 2010, **2**, 901376.
7. C. Wu, C. Liu, Y. Tao, Y. Zhang and Y. Chen, *Phys. Lett. A*, 2020, **384**, 126751.
8. B. Wu, Y. Guo, C. Hou, Q. Zhang, Y. Li and H. Wang, *Adv. Funct. Mater.*, 2019, **29**, 1900304.
9. C. Chang, M. Wu, D. He, Y. Pei, C.-F. Wu, X. Wu, H. Yu, F. Zhu, K. Wang, Y. Chen, L. Huang, J.-F. Li, J. He and L.-D. Zhao, *Science*, 2018, **360**, 778-783.
10. S. Ondaral, O. Kurtuluş, G. Öztürk, M. Ergün and İ. Yakın, *BioRes.*, 2018, **13**, 4470-4483.
11. Q. Zhang, W. Wang, J. Li, J. Zhu, L. Wang, M. Zhu and W. Jiang, *J. Mater. Chem. A*, 2013, **1**, 12109-12114.
12. Q. Hu, Z. Lu, Y. Wang, J. Wang, H. Wang, Z. Wu, G. Lu, H.-L. Zhang and C. Yu, *J. Mater. Chem. A*, 2020, **8**, 13095-13105.
13. Y. Nakashima, R. Yamaguchi, F. Toshimitsu, M. Matsumoto, A. Borah, A. Staykov, M. S. Islam, S. Hayami and T. Fujigaya, *ACS Appl. Nano Mater.*, 2019, **2**, 4703-4710.
14. R. A. Schlitz, F. G. Brunetti, A. M. Glaudell, P. L. Miller, M. A. Brady, C. J. Takacs, C. J. Hawker and M. L. Chabinyc, *Adv. Mater.*, 2014, **26**, 2825-2830.
15. I. Loa, *J. Raman Spectrosc.*, 2003, **34**, 611-627.
16. M. Hu, Z. Zhao, F. Tian, A. R. Oganov, Q. Wang, M. Xiong, C. Fan, B. Wen, J. He, D. Yu, H.-T. Wang, B. Xu and Y. Tian, *Sci. Rep.*, 2013, **3**, 1331.
17. C. Chen, Y. Lin, W. Zhou, M. Gong, Z. He, F. Shi, X. Li, J. Z. Wu, K. T. Lam, J. N. Wang, F. Yang, Q. Zeng, J. Guo, W. Gao, J.-M. Zuo, J. Liu, G. Hong, A. L. Antaris, M.-C. Lin, W. L. Mao and H. Dai, *Nat. Electron.*, 2021, **4**, 653-663.
18. Y. Wang, Z. Lu, Q. Hu, X. Qi, Q. Li, Z. Wu, H.-L. Zhang, C. Yu and H. Wang, *J. Mater. Chem. A*, 2021, **9**, 3341-3352.
19. D. Huang, H. Yao, Y. Cui, Y. Zou, F. Zhang, C. Wang, H. Shen, W. Jin, J. Zhu, Y. Diao, W. Xu, C.-a. Di and D. Zhu, *J. Am. Chem. Soc*, 2017, **139**, 13013-13023.
20. H.-I. Un, S. A. Gregory, S. K. Mohapatra, M. Xiong, E. Longhi, Y. Lu, S. Rigin, S. Jhulki, C.-Y. Yang, T. V. Timofeeva, J.-Y. Wang, S. K. Yee, S. Barlow, S. R. Marder and J. Pei, *Adv. Energy Mater.*, 2019, **9**, 1900817.
21. D. Kiefer, A. Giovannitti, H. Sun, T. Biskup, A. Hofmann, M. Koopmans, C. Cendra, S. Weber, L. J. Anton Koster, E. Olsson, J. Rivnay, S. Fabiano, I. McCulloch and C. Müller, *ACS Energy Lett.*, 2018, **3**, 278-285.
22. S. El Oualid, I. Kogut, M. Benyahia, E. Geczi, U. Kruck, F. Kosior, P. Masschelein, C. Candolfi, A. Dauscher, J. D. Koenig, A. Jacquot, T. Caillat, E. Alleno and B. Lenoir, *Adv. Energy Mater.*, 2021, **11**, 2100580.
23. W. Zhou, Q. Fan, Q. Zhang, L. Cai, K. Li, X. Gu, F. Yang, N. Zhang, Y. Wang, H. Liu, W. Zhou and S. Xie, *Nat. Commun.*, 2017, **8**, 14886.
24. T. Sun, B. Zhou, Q. Zheng, L. Wang, W. Jiang and G. J. Snyder, *Nat. Commun.*, 2020, **11**, 572.
25. K. Suemori and S. Uemura, *Appl. Phys. Lett.*, 2020, **116**, 081902.
26. D. Li, C. Luo, Y. Chen, D. Feng, Y. Gong, C. Pan and J. He, *ACS Appl. Energy Mater.*, 2019, **2**,

2427-2434.
27. M. Nakano, T. Nakashima, T. Kawai and Y. Nonoguchi, *Small*, 2017, **13**, 1700804.
28. J.-Y. Kim, J.-H. Mo, Y. H. Kang, S. Y. Cho and K.-S. Jang, *Nanoscale*, 2018, **10**, 19766-19773.
29. P. Li, Y. Zhao, H. Li, S. Liu, Y. Liang, X. Cheng and C. He, *Compos. Sci. Technol.*, 2020, **189**, 108023.
30. W. Fan, L. Liang, B. Zhang, C.-Y. Guo and G. Chen, *J. Mater. Chem. A*, 2019, **7**, 13687-13694.
31. L. Wei, H. Huang, C. Gao, D. Liu and L. Wang, *Mater. Horizons*, 2021, **8**, 1207-1215.
32. W. Fan, Y. Zhang, C.-Y. Guo and G. Chen, *Compos. Sci. Technol.*, 2019, **183**, 107794.
33. H. Wang, S.-i. Yi, X. Pu and C. Yu, *ACS Appl. Mater. Interfaces*, 2015, **7**, 9589-9597.
34. Y. Zhou, Y. Liu, X. Zhou, Y. Gao, C. Gao and L. Wang, *J. Power Sources*, 2019, **423**, 152-158.
35. N. Feng, C. Gao, C.-Y. Guo and G. Chen, *ACS Appl. Mater. Interfaces*, 2018, **10**, 5603-5608.
36. W. Deng, L. Deng, Z. Li, Y. Zhang and G. Chen, *ACS Appl. Mater. Interfaces*, 2021, **13**, 12131-12140.
37. Z. Chen, T. Liu, C. Pan and G. Tan, *Polymers*, 2020, **12**, 848.
38. C. Yu, K. Choi, L. Yin and J. C. Grunlan, *ACS Nano*, 2011, **5**, 7885-7892.
39. L. Wang, J. Zhang, Y. Guo, X. Chen, X. Jin, Q. Yang, K. Zhang, S. Wang and Y. Qiu, *Carbon*, 2019, **148**, 290-296.
40. W. Fan, C.-Y. Guo and G. Chen, *J. Mater. Chem. A*, 2018, **6**, 12275-12280.
41. L. Liang, X. Wang, M. Wang, Z. Liu, G. Chen and G. Sun, *Compos. Commun.*, 2021, **25**, 100701.
42. Z. Li, L. Deng, H. Lv, L. Liang, W. Deng, Y. Zhang and G. Chen, *Adv. Funct. Mater.*, 2021, **31**, 2104836.
43. W. Lu, Q. Luo, S. Yin, X. Wu and C.-Y. Guo, *Compos. Commun.*, 2021, **27**, 100860.
44. P. Cataldi, M. Cassinelli, J. A. Heredia-Guerrero, S. Guzman-Puyol, S. Naderizadeh, A. Athanassiou and M. Caironi, *Adv. Funct. Mater.*, 2020, **30**, 1907301.
45. X. Nie, X. Mao, X. Li, J. Wu, Y. Liu, B. Li, L. Xiang, C. Gao, Y. Xie and L. Wang, *Chem. Eng. J.*, 2021, **421**, 129718.
46. Y. Liu, Q. Dai, Y. Zhou, B. Li, X. Mao, C. Gao, Y. Gao, C. Pan, Q. Jiang, Y. Wu, Y. Xie and L. Wang, *ACS Appl. Mater. Interfaces*, 2019, **11**, 29320-29329.
47. X. Mao, Z. Li, Y. Liu, X. Nie, B. Li, Q. Jiang, C. Gao, Y. Gao and L. Wang, *Chem. Eng. J.*, 2021, **405**, 126616.
48. X. Cheng, X. Wang and G. Chen, *J. Mater. Chem. A*, 2018, **6**, 19030-19037.
49. S. Wang, J. Wu, F. Yang, H. Xin, L. Wang and C. Gao, *ACS Appl. Mater. Interfaces*, 2021, **13**, 26482-26489.
50. G. Wu, Z.-G. Zhang, Y. Li, C. Gao, X. Wang and G. Chen, *ACS Nano*, 2017, **11**, 5746-5752.
51. J.-Y. Kim, W. Lee, Y. H. Kang, S. Y. Cho and K.-S. Jang, *Carbon*, 2018, **133**, 293-299.
52. C. Gao, Y. Liu, Y. Gao, Y. Zhou, X. Zhou, X. Yin, C. Pan, C. Yang, H. Wang, G. Chen and L. Wang, *J. Mater. Chem. A*, 2018, **6**, 20161-20169.
53. S. Qin, J. Tan, J. Qin, J. Luo, J. Jin, S. Huang, L. Wang and D. Liu, *Adv. Electronic Mater.*, 2021, **7**, 2100557.
54. Y. Nonoguchi, Y. Iihara, K. Ohashi, T. Murayama and T. Kawai, *Chem. Asian. J.*, 2016, **11**, 2423-2427.
55. X. Nie, X. Li, Y. Huang, J. Wu, F. Yang, F. Zhong, X. Hong, C. Gao and L. Wang, *Compos. Commun.*, 2021, **27**, 100873.

56. Y. Wang, Z. Chen, H. Huang, D. Wang, D. Liu and L. Wang, *J. Mater. Chem. A*, 2020, **8**, 24675-24684.
57. J.-H. Mo, J.-Y. Kim, Y. H. Kang, S. Y. Cho and K.-S. Jang, *ACS Sustain. Chem. Eng.*, 2018, **6**, 15970-15975.
58. C. Yu, A. Murali, K. Choi and Y. Ryu, *Energy Environ. Sci.*, 2012, **5**, 9481-9486.
59. J. Kim, O. H. Kwon, Y. H. Kang, K.-S. Jang, S. Y. Cho and Y. Yoo, *Compos. Sci. Technol.*, 2017, **153**, 32-39.
60. G. Wu, C. Gao, G. Chen, X. Wang and H. Wang, *J. Mater. Chem. A*, 2016, **4**, 14187-14193.
61. Y. Liu, D. R. Villalva, A. Sharma, M. A. Haque and D. Baran, *ACS Appl. Mater. Interfaces*, 2021, **13**, 411-418.
62. D. Abol-Fotouh, B. Dörling, O. Zapata-Arteaga, X. Rodríguez-Martínez, A. Gómez, J. S. Reparaz, A. Laromaine, A. Roig and M. Campoy-Quiles, *Energy Environ. Sci.*, 2019, **12**, 716-726.
63. C.-K. Mai, B. Russ, S. L. Fronk, N. Hu, M. B. Chan-Park, J. J. Urban, R. A. Segalman, M. L. Chabinyc and G. C. Bazan, *Energy Environ. Sci.*, 2015, **8**, 2341-2346.
64. Y. Lei, R. Qi, M. Chen, H. Chen, C. Xing, F. Sui, L. Gu, W. He, Y. Zhang, T. Baba, T. Baba, H. Lin, T. Mori, K. Koumoto, Y. Lin and Z. Zheng, *Adv. Mater.*, 2022, **34**, 2104786.
65. C. Jiang, P. Wei, Y. Ding, K. Cai, L. Tong, Q. Gao, Y. Lu, W. Zhao and S. Chen, *Nano Energy*, 2021, **80**, 105488.
66. C. J. An, Y. H. Kang, H. Song, Y. Jeong and S. Y. Cho, *J. Mater. Chem. A*, 2017, **5**, 15631-15639.
67. K. T. Park, Y. S. Cho, I. Jeong, D. Jang, H. Cho, Y. Choi, T. Lee, Y. Ko, J. Choi, S. Y. Hong, M.-W. Oh, S. Chung, C. R. Park and H. Kim, *Adv. Energy Mater.*, 2022, **n/a**, 2200256.
68. X. Li, Y. Lu, K. Cai, M. Gao, Y. Li, Z. Wang, M. Wu, P. Wei, W. Zhao, Y. Du and S. Shen, *Chem. Eng. J.*, 2022, **434**, 134739.
69. T. Varghese, C. Hollar, J. Richardson, N. Kempf, C. Han, P. Gamarachchi, D. Estrada, R. J. Mehta and Y. Zhang, *Sci. Rep.*, 2016, **6**, 33135.
70. S. Kim, J.-H. Mo and K.-S. Jang, *ACS Appl. Mater. Interfaces*, 2020, **12**, 43778-43784.
71. Q. Xu, S. Qu, C. Ming, P. Qiu, Q. Yao, C. Zhu, T.-R. Wei, J. He, X. Shi and L. Chen, *Energy Environ. Sci.*, 2020, **13**, 511-518.
72. S. Qu, C. Ming, P. Qiu, K. Xu, Q. Xu, Q. Yao, P. Lu, H. Zeng, X. Shi and L. Chen, *Energy Environ. Sci.*, 2021, **14**, 6586-6594.
73. X. Sun, Y. Wang, K. Li, J. Wang, X. Dai, D. Chong, J. Yan and H. Wang, *Adv. Funct. Mater.*, 2022, **n/a**, 2203080.
74. Y. Lu, Y. Qiu, K. Cai, X. Li, M. Gao, C. Jiang and J. He, *Mater. Today Phys.*, 2020, **14**, 100223.
75. V. Karthikeyan, J. U. Surjadi, J. C. K. Wong, V. Kannan, K.-H. Lam, X. Chen, Y. Lu and V. A. L. Roy, *J. Power Sources*, 2020, **455**, 227983.
76. T. Lee, J. W. Lee, K. T. Park, J.-S. Kim, C. R. Park and H. Kim, *ACS Nano*, 2021, **15**, 13118-13128.
77. J. Choi, Y. Jung, S. J. Yang, J. Y. Oh, J. Oh, K. Jo, J. G. Son, S. E. Moon, C. R. Park and H. Kim, *ACS Nano*, 2017, **11**, 7608-7614.
78. E. J. Bae, Y. H. Kang, C. Lee and S. Y. Cho, *J. Mater. Chem. A*, 2017, **5**, 17867-17873.
79. Y. Lu, Y. Qiu, K. Cai, Y. Ding, M. Wang, C. Jiang, Q. Yao, C. Huang, L. Chen and J. He, *Energy Environ. Sci.*, 2020, **13**, 1240-1249.

80. Y. Ding, Y. Qiu, K. Cai, Q. Yao, S. Chen, L. Chen and J. He, *Nat. Commun.*, 2019, **10**, 841.
81. C. Liu, D.-L. Shan, Z.-H. Shen, G.-K. Ren, W. Yue, Z.-F. Zhou, J.-Y. Li, D. Yi, J.-L. Lan, L.-Q. Chen, G. J. Snyder, Y.-H. Lin and C.-W. Nan, *Nano Energy*, 2021, **89**, 106380.
82. K. T. Park, J. Choi, B. Lee, Y. Ko, K. Jo, Y. M. Lee, J. A. Lim, C. R. Park and H. Kim, *J. Mater. Chem. A*, 2018, **6**, 19727-19734.
83. L. Liang, M. Wang, X. Wang, P. Peng, Z. Liu, G. Chen and G. Sun, *Adv. Funct. Mater.*, 2022, **32**, 2111435.
84. B. Wu, Y. Guo, C. Hou, Q. Zhang, Y. Li and H. Wang, *Nano Energy*, 2021, **89**, 106487.
85. C. K. Mytafides, L. Tzounis, G. Karalis, P. Formanek and A. S. Paipetis, *J. Power Sources*, 2021, **507**, 230323.
86. D. Qu, X. Huang, X. Li, H. Wang and G. Chen, *npj Flex. Electron.*, 2020, **4**, 1.
87. S. Yin, X. Wu, R. Wang and C.-Y. Guo, *Macromol. Mater. Eng.*, 2022, **n/a**, 2200094.
88. W. Zhao, S. Fan, N. Xiao, D. Liu, Y. Y. Tay, C. Yu, D. Sim, H. H. Hng, Q. Zhang, F. Boey, J. Ma, X. Zhao, H. Zhang and Q. Yan, *Energy Environ. Sci.*, 2012, **5**, 5364-5369.
89. D. Kim, Y. Park, D. Ju, G. Lee, W. Kwon and K. Cho, *Chem. Mater.*, 2021, **33**, 4853-4862.
90. K. Oshima, J. Inoue, S. Sadakata, Y. Shiraishi and N. Toshima, *J. Electron. Mater.*, 2017, **46**, 3207-3214.
91. N. Toshima, K. Oshima, H. Anno, T. Nishinaka, S. Ichikawa, A. Iwata and Y. Shiraishi, *Adv. Mater.*, 2015, **27**, 2246-2251.
92. Y. Li, C.-Y. Gao, X.-H. Fan and L.-M. Yang, *Chem. Eng. J.*, 2022, **443**, 136536.
93. L. Zhang, Y. Harima and I. Imae, *Org. Electron*, 2017, **51**, 304-307.
94. Q. Yao, Q. Wang, L. Wang and L. Chen, *Energy Environ. Sci.*, 2014, **7**, 3801-3807.
95. B. A. MacLeod, N. J. Stanton, I. E. Gould, D. Wesenberg, R. Ihly, Z. R. Owczarczyk, K. E. Hurst, C. S. Fewox, C. N. Folmar, K. Holman Hughes, B. L. Zink, J. L. Blackburn and A. J. Ferguson, *Energy Environ. Sci.*, 2017, **10**, 2168-2179.
96. Q. Jiang, X. Lan, C. Liu, H. Shi, Z. Zhu, F. Zhao, J. Xu and F. Jiang, *Mater. Chem. Front.* , 2018, **2**, 679-685.
97. Y. Nonoguchi, K. Ohashi, R. Kanazawa, K. Ashiba, K. Hata, T. Nakagawa, C. Adachi, T. Tanase and T. Kawai, *Sci. Rep.*, 2013, **3**, 3344.
98. Y. Chen, Q. Yao, S. Qu, W. Shi, H. Li and L. Chen, *ACS Appl. Mater. Interfaces*, 2021, **13**, 55156-55163.
99. F. Jia, R. Wu, C. Liu, J. Lan, Y.-H. Lin and X. Yang, *ACS Sustain. Chem. Eng.*, 2019, **7**, 12591-12600.
100. L. Wang, C. Pan, Z. Chen, W. Zhou, C. Gao and L. Wang, *ACS Appl. Energy Mater.*, 2018, **1**, 5075-5082.
101. G. H. Kim, D. H. Hwang and S. I. Woo, *Phys. Chem. Chem. Phys*, 2012, **14**, 3530-3536.
102. C. A. Hewitt, A. B. Kaiser, S. Roth, M. Craps, R. Czerw and D. L. Carroll, *Nano Lett.*, 2012, **12**, 1307-1310.
103. Y. Xue, Z. Zhang, Y. Zhang, X. Wang, L. Li, H. Wang and G. Chen, *Carbon*, 2020, **157**, 324-329.
104. D. Kim, Y. Kim, K. Choi, J. C. Grunlan and C. Yu, *ACS Nano*, 2010, **4**, 513-523.
105. K. Chatterjee, A. Negi, K. Kim, J. Liu and T. K. Ghosh, *ACS Appl. Energy Mater.*, 2020, **3**, 6929-6936.
106. C. Bounioux, P. Díaz-Chao, M. Campoy-Quiles, M. S. Martín-González, A. R. Goñi, R.

Yerushalmi-Rozen and C. Müller, *Energy Environ. Sci.*, 2013, **6**, 918-925.
107. S. Hata, J. Tomotsu, M. Gotsubo, Y. Du, Y. Shiraishi and N. Toshima, *Polym. J.*, 2021, **53**, 1281-1286.
108. X.-z. Jin, H. Li, Y. Wang, Z.-y. Yang, X.-d. Qi, J.-h. Yang and Y. Wang, *ACS Appl. Mater. Interfaces*, 2022, **14**, 27083-27095.
109. K. Zhang, M. Davis, J. Qiu, L. Hope-Weeks and S. Wang, *Nanotechnology*, 2012, **23**, 385701.
110. M. H. Kim, C. H. Cho, J. S. Kim, T. U. Nam, W.-S. Kim, T. Il Lee and J. Y. Oh, *Nano Energy*, 2021, **87**, 106156.
111. Y. Nonoguchi, M. Nakano, T. Murayama, H. Hagino, S. Hama, K. Miyazaki, R. Matsubara, M. Nakamura and T. Kawai, *Adv. Funct. Mater.*, 2016, **26**, 3021-3028.
112. X. Qi, Y. Wang, K. Li, J. Wang, H.-L. Zhang, C. Yu and H. Wang, *J. Mater. Chem. A*, 2021, **9**, 310-319.
113. D. Tan, J. Zhao, C. Gao, H. Wang, G. Chen and D. Shi, *ACS Appl. Mater. Interfaces*, 2017, **9**, 21820-21828.
114. Y. H. Kang, E. J. Bae, M.-H. Lee, M. Han, B. J. Kim and S. Y. Cho, *Small*, 2022, **18**, 2106108.
115. Y. Liu, D. R. Villalva, A. Sharma, M. A. Haque and D. Baran, *ACS Applied Materials & Interfaces*, 2021, **13**, 411-418.
116. Y. H. Kang, Y.-C. Lee, C. Lee and S. Y. Cho, *Org. Electron*, 2018, **57**, 165-170.
117. J. G. Jang, S. Y. Woo, H. Lee, E. Lee, S. H. Kim and J.-I. Hong, *ACS Appl. Mater. Interfaces*, 2020, **12**, 51387-51396.
118. P. Fu, J.-K. Xiao, J.-Z. Gong, Y. Zhu, J.-A. Yao, Y.-F. Zhang, S.-G. Wang, Z.-D. Lin and F.-P. Du, *Synth. Met.*, 2021, **280**, 116861.
119. S. Horike, Q. Wei, K. Akaike, K. Kirihara, M. Mukaida, Y. Koshiba and K. Ishida, *Nat. Commun.*, 2022, **13**, 3517.
120. J.-H. Mo, J.-Y. Kim, Y. H. Kang, S. Y. Cho and K.-S. Jang, *ACS Sustainable Chemistry & Engineering*, 2018, **6**, 15970-15975.
121. L. Wang, X. Jia, D. Wang, G. Zhu and J. Li, *Synth. Met.*, 2013, **181**, 79-85.
122. S. Park, J.-H. Mo, S. Kim, H. Hwang and K.-S. Jang, *ACS Appl. Mater. Interfaces*, 2020, **12**, 19415-19422.
123. M. Gnanaseelan, Y. Chen, J. Luo, B. Krause, J. Pionteck, P. Pötschke and H. Qi, *Compos. Sci. Technol.*, 2018, **163**, 133-140.
124. X. Zhou, C. Pan, A. Liang, L. Wang, T. Wan, G. Yang, C. Gao and W. Y. Wong, *J. Appl. Polym. Sci.*, 2019, **136**, 47011.
125. B. Krause, A. Liguoro and P. Pötschke, *Nanomaterials*, 2021, **11**.
126. B. Krause, V. Bezugly, V. Khavrus, L. Ye, G. Cuniberti and P. Pötschke, *Energies*, 2020, **13**.